The formation of disc galaxies in high resolution moving-mesh cosmological simulations

Federico Marinacci[1,2], Rüdiger Pakmor[1] and Volker Springel[1,2]

[1] *Heidelberger Institut für Theoretische Studien, Schloss-Wolfsbrunnenweg 35, D-69118 Heidelberg, Germany*
[2] *Zentrum für Astronomie der Universität Heidelberg, Astronomisches Recheninstitut, Mönchhofstr. 12-14, D-69120 Heidelberg, Germany*

ABSTRACT
We present cosmological hydrodynamical simulations of eight Milky Way-sized haloes that have been previously studied with dark matter only in the Aquarius project. For the first time, we employ the moving-mesh code AREPO in zoom simulations combined with a comprehensive model for galaxy formation physics designed for large cosmological simulations. Our simulations form in most of the eight haloes strongly disc-dominated systems with realistic rotation curves, close to exponential surface density profiles, a stellar-mass to halo-mass ratio that matches expectations from abundance matching techniques, and galaxy sizes and ages consistent with expectations from large galaxy surveys in the local Universe. There is no evidence for any dark matter core formation in our simulations, even so they include repeated baryonic outflows by supernova-driven winds and black hole quasar feedback. For one of our haloes, the object studied in the recent 'Aquila' code comparison project, we carried out a resolution study with our techniques, covering a dynamic range of 64 in mass resolution. Without any change in our feedback parameters, the final galaxy properties are reassuringly similar, in contrast to other modelling techniques used in the field that are inherently resolution dependent. This success in producing realistic disc galaxies is reached, in the context of our interstellar medium treatment, without resorting to a high density threshold for star formation, a low star formation efficiency, or early stellar feedback, factors deemed crucial for disc formation by other recent numerical studies.

Key words: methods: numerical – galaxies: evolution – galaxies: formation – galaxies: spiral

1 INTRODUCTION

Forming realistic disc galaxies in self-consistent hydrodynamical simulations of the Λ cold dark matter (ΛCDM) cosmology has been a nagging problem for more than two decades (after pioneering work by Katz & Gunn 1991). In stark contrast to the successes reached with dark matter only simulations of cosmic large-scale structure (e.g. Davis et al. 1985; Springel et al. 2006) and with semi-analytic galaxy formation models (e.g. Guo et al. 2011), making *realistic* spiral galaxies on the computer has emerged as an unexpectedly difficult endeavour that has withstood countless attempts at solving it over the years. Instead, the simulated galaxies were often too small due to an angular momentum deficit (e.g. Navarro & Steinmetz 2000), they featured at best anaemic discs and almost universally too concentrated and massive bulges (e.g. Scannapieco et al. 2009), their rotation curves had unrealistic shapes (e.g. Hummels & Bryan 2012), and in general they were far too luminous (e.g. Mar-

tig et al. 2012) as a result of the "overcooling catastrophe" (Balogh et al. 2001).

Recently, however, the situation has profoundly changed, and there are now several studies that obtained disc galaxies in quite reasonable agreement with key observables (Governato et al. 2010; Agertz et al. 2011; Brooks et al. 2011; Guedes et al. 2011; Aumer et al. 2013; Stinson et al. 2013a). In particular, for the first time, we have seen simulations that produce reasonably small bulges and a dominant disc, combined with realistic rotation curves, roughly correct sizes, and low enough stellar masses to be compatible with abundance matching expectations (Aumer et al. 2013; Stinson et al. 2013a). This progress raises the question of what cut the Gordian knot that had allowed only incremental advances for many years (Governato et al. 2004, 2007; Robertson et al. 2004; Scannapieco et al. 2008, 2009, 2011; Sales et al. 2009, 2010; Stinson et al. 2010; Piontek & Steinmetz 2011).

There are different claims in the literature about the

key remedy for the impasse. Some studies have argued that very high numerical resolution is a central and potentially sufficient requirement (e.g. Governato et al. 2007; Kaufmann et al. 2007), whereas other works emphasized that the degree of success critically depends on the modelling of the physics of star formation and feedback (e.g. Okamoto et al. 2005; Scannapieco et al. 2008; Sales et al. 2010). Recently, some authors suggested that a high star formation threshold is a key factor in allowing the successful formation of a late-type spiral galaxy like the Milky Way (Guedes et al. 2011). On the other hand, Agertz et al. (2011) find that a low star-formation efficiency, particularly at high redshift, is important, whereas an opposite conclusion was reached by Sommer-Larsen et al. (2003) and Sales et al. (2010), who favoured a high star formation efficiency instead. Other studies pointed out that additional feedback channels such as cosmic rays (e.g. Uhlig et al. 2012), or stellar evolutionary processes in the form of mass return (Leitner & Kravtsov 2011) need to be considered.

Which of these factors reflects essential physics important for disc formation rather than numerics or the particularities of a specific modelling technique is far from clear. A recurrent theme, though, is that in all the recent successful simulations of disc galaxies a much stronger feedback than employed in previous calculations is invoked. In particular, the advances in reproducing disc galaxies by Stinson et al. (2013a) and Aumer et al. (2013) are attributed to 'early stellar feedback' introduced by the authors. In the actual numerical implementation of Stinson et al. (2013a), this form of feedback is injecting considerably more energy than from supernovae alone and allows the simulations to finally curtail the overproduction of stars at high redshift that invariably led to an excessively massive central bulge component later on. Whether the adopted subgrid modelling of the physics of radiation pressure of newly born stars is realistic has to be seen, but optimistic assumptions about the efficiency of feedback are needed by all authors to reduce early star formation and delay disc formation to sufficiently late times.

Indeed, perhaps the most general lesson of recent simulation work on galaxy formation is that the importance of feedback for the outcome of hydrodynamical cosmological simulations can hardly be overstated. The Aquila comparison project (Scannapieco et al. 2012) has shown that different numerical codes can give widely different outcomes for the same initial conditions. Even the same code can give substantially different answers if small details in the implementation of feedback and star formation physics are changed. Many feedback implementations in current use are not robust to resolution changes and require 'retuning' of the free parameters of the model to obtain the same or a similar result when the resolution is changed – if at all possible. The differences can be as extreme as those reported in Okamoto et al. (2005), where a galaxy's morphology simulated at different resolution varied over the entire range of Hubble types. Part of this sensitivity to small model and simulation details can be attributed to the highly non-linear nature of the feedback loops that need to drastically reduce star formation both in small and large haloes. This is already a significant complication for strong supernova-driven winds but is especially evident for active galactic nuclei (AGN) feedback (Springel et al. 2005a). For some periods of time, black holes (BHs) are expected to grow exponentially, a process that can hugely amplify any tiny numerical differences of the conditions around the BH that set the accretion rate.

However, part of the lack of robustness in simulation outcomes certainly also needs to be blamed on numerical models that are essentially ill posed, in the sense that the feedback prescriptions used are often heuristic, and not derived rigorously as a discretization of some well-defined partial differential equations that approximate the physics. As a result, the response of the models to resolution changes is poorly defined and sometimes not well understood, as some studies candidly concede (e.g. Stinson et al. 2006; Aumer et al. 2013). This often reflects a fuzzy notion of how 'subgrid' physics (which invariably plays an important role in this problem) should be treated, or sometimes an ignorance of this unavoidable limitation altogether. We argue in this paper that resolution-dependent feedback implementations make it hard to separate physics from numerical effects, and we hence advocate the use of more explicit subgrid models.

Even at the level of the ordinary hydrodynamical equations that describe an ideal gas, simulation results can be strongly affected by the numerical scheme employed for solving hydrodynamics, as emphasized recently (Kereš et al. 2012; Sijacki et al. 2012; Torrey et al. 2012; Vogelsberger et al. 2012). These studies have shown that accuracy differences between smoothed particle hydrodynamics (SPH, as implemented in the GADGET code) and the moving-mesh approach of the AREPO code directly translate into sizable changes of predicted galaxy properties. In fact, there is an artificial numerical quenching of the cooling rate in large haloes in SPH, caused by viscosity and noise effects (Bauer & Springel 2012). The standard formulation of SPH also creates spurious dense gas clumps orbiting in haloes. This greatly modifies how galaxies acquire their gas in large haloes, suppressing the relative importance of hot mode gas accretion in these systems (Nelson et al. 2013).

Unfortunately, the size of these numerical uncertainties is so large that they can mask important physical processes and induce incorrect calibrations of the required feedback strength. It is therefore important to use an as accurate numerical technique for hydrodynamics as is available. Similarly, sensitive dependences on fine details of feedback implementations, especially with respect to numerical resolution, are highly undesirable as this will add to the difficulty of separating physics from numerics, and ultimately compromise the predictive power of the simulations. Hence, we argue that a crucial requirement for the current generation of cosmological simulations of galaxy formation is that their numerical models should be sufficiently well posed to yield results approximately invariant with numerical resolution, at least over a reasonable range where crucial physics remains subgrid and can only be treated in a phenomenological way. To our knowledge, this requirement is not yet fulfilled by the reported successful simulations of disc galaxy formation in the recent literature.

In this paper, we study the problem by applying a newly developed numerical methodology for cosmological galaxy formation to 'zoom' simulations of Milky Way-sized galaxies. The objects we study are taken from the Aquarius project (Springel et al. 2008), where they have been examined in great detail with dark matter only simulations. We added two further haloes to the Aquarius set which were not run at high resolution in the original project but were still part

of its target list. This same extended set of Milky Way-sized haloes has been previously studied with hydrodynamics by Scannapieco et al. (2009) using SPH, which hence serves as an interesting comparison for our results. One of the Aquarius haloes, the 'Aq-C' system, has been the object selected for the Aquila code comparison project (Scannapieco et al. 2012), yielding another reference for direct comparisons. Finally, a subset of the Aquarius systems has been simulated very recently by Aumer et al. (2013) with an updated SPH code (based on Scannapieco et al. 2009), yielding considerably improved results, in particular with respect to the disc-to-bulge (D/B) ratio and the total stellar mass.

The novel simulation methodology we apply to all eight haloes consists of our moving-mesh code AREPO (Springel 2010) combined with a comprehensive model for the galaxy formation physics, as described in full detail in Vogelsberger et al. (2013). We also include a resolution study by considering both a higher and a lower resolution run by a factor of 8 in mass around the nominal resolutions of Scannapieco et al. (2009) and Aumer et al. (2013), which is equal to the default resolution that we have picked here. Our primary goal is to investigate whether our new numerical treatments yield reasonable galaxy morphologies and properties in these systems, despite the fact that we do not use a high density threshold for star formation, a low star formation efficiency, or early stellar feedback – or in other words, some of the ingredients that have been deemed essential by other studies for successfully forming disc galaxies.

This paper is structured as follows. In Section 2, we briefly summarize the numerical methodology used in our moving-mesh simulations, and we detail the simulation set that we examine. In Section 3, we analyse the present-day structures of the galaxies that we obtain in the Aquarius haloes, including an analysis of their gas content. In Section 4, we turn to an analysis of the formation history of the galaxies, both in terms of their stars and their embedded supermassive BHs. A brief analysis of the halo mass structure and the impact of baryonic physics on the dark matter distribution is given in Section 5, followed by results of a resolution study in Section 6. Finally, we discuss our findings and present our conclusions in Section 7.

2 NUMERICAL METHODOLOGY AND SIMULATION SET

2.1 Initial conditions

We use initial conditions from the Aquarius suite of high-resolution dark matter simulations of Milky Way-sized haloes (Springel et al. 2008). The simulated volume is a periodic cube with a side length of $100\,h^{-1}$Mpc. The adopted ΛCDM cosmology uses the parameters $\Omega_{\rm m} = \Omega_{\rm dm} + \Omega_{\rm b} = 0.25$, $\Omega_{\rm b} = 0.04$, $\Omega_{\Lambda} = 0.75$, $\sigma_8 = 0.9$, $n_s = 1$, and a Hubble constant of $H_0 = 100\,h\,{\rm km\,s^{-1}\,Mpc^{-1}} = 73\,{\rm km\,s^{-1}\,Mpc^{-1}}$. These cosmological parameters are the same as in the Millennium and Millennium-II simulations (Springel et al. 2005b; Boylan-Kolchin et al. 2009). While they are now in tension with the diminished error bars of the latest cosmological constraints from the *Wilkinson Microwave Anisotropy Probe* and *Planck* satellites, this is of no relevance for this study. In order to achieve the high resolution needed to resolve the formation of a Milky Way-like

galaxy, our initial conditions utilize the 'zoom-in technique', i.e. the Lagrangian region from which the main galaxy forms is sampled with a high number of low-mass particles whereas the rest of the simulation volume is filled with progressively higher mass particles whose mass grows with distance from the target galaxy. This saves computational time while still ensuring the correct cosmological tidal field and mass infall rate for the forming target galaxy.

The target galaxies themselves have been selected randomly from a small mass interval around $10^{12}\,{\rm M_\odot}$, applying only a rather mild isolation criterion that excluded objects close to another massive galaxy. Specifically, haloes with mass greater than half that of the candidate object were required to be at least $1.37\,$Mpc away from the candidate halo at $z = 0$. This weak criterion is not very restrictive; it was not met by about 22% of the haloes from the purely mass-selected sample, but it still helps to preferentially select galaxies with quiet merger histories which are expected to be favourable sites for producing late-type galaxies. A detailed analysis of the formation history of the selected haloes and the scatter among the set can be found in Boylan-Kolchin et al. (2010).

We note that recent estimates of the mass of the Galaxy's dark matter halo range from 1 to 3×10^{12} (Wilkinson & Evans 1999; Sakamoto et al. 2003; Battaglia et al. 2005; Dehnen et al. 2006; Li & White 2008; Xue et al. 2008). In order to alleviate tensions due to the 'missing massive satellites problem' pointed out by Boylan-Kolchin et al. (2011, 2012), a recent analysis by Wang et al. (2012) favours masses at the lower end of this interval, at around $10^{12}\,{\rm M_\odot}$, which is also the centre of the narrow mass interval that we study. On the other hand, using the space motion of the Leo I dwarf spheroidal galaxy, Boylan-Kolchin et al. (2013) put a strong lower limit on the Milky Way's mass, finding a median mass of $1.6 \times 10^{12}\,{\rm M_\odot}$, rather similar to several of our candidate systems.

Following the nomenclature used in the Aquarius project, the primary simulations that we carry out are hydrodynamical versions of Aq-A-5, Aq-B-5, Aq-C-5, Aq-D-5, Aq-E-5, Aq-F-5, Aq-G-5, and Aq-H-5. Here the '5' in the name refers to the resolution level, corresponding to a baryonic mass resolution of $\sim 4.1 \times 10^5\,{\rm M_\odot}$ and a dark matter mass resolution of $\sim 2.2 \times 10^6\,{\rm M_\odot}$ (for Aq-C-5). At $z > 1$, we keep the gravitational softening length of all mass components in the high-resolution region constant in comoving units, growing the physical gravitational softening length to a maximum of $680\,$pc, which was then held constant for $z \leq 1$. In our resolution study of the Aq-C halo (which is the object studied in the Aquila comparison project), we also consider simulations adopting a baryonic mass resolution of $3.2 \times 10^6\,{\rm M_\odot}$ with a gravitational softening of 1.36 kpc, as well as $5 \times 10^4\,{\rm M_\odot}$ with a gravitational softening length of 340 pc, which correspond to mass resolutions of a factor of 8 better or worse (equivalent to levels 4 and 6 in the Aquarius project) than our default, respectively. We note that these softening values follow the optimum choices derived by Power et al. (2003). Smaller softening values would lead to significant two-body effects and a spurious heating of the gas, particularly at high redshift, and are hence not well justified.

In Table 1, we list the principal numerical parameters

Run	$R_{\rm vir}$ (kpc)	$M_{\rm tot}$ $(10^{10}{\rm M}_\odot)$	$M_{\rm gas}$ $(10^{10}{\rm M}_\odot)$	$M_\star$ $(10^{10}{\rm M}_\odot)$	$M_{\rm dm}$ $(10^{10}{\rm M}_\odot)$	$N_{\rm cells}$	$N_\star$	$N_{\rm dm}$	$m_{\rm gas}$ $(10^5{\rm M}_\odot)$	$m_{\rm dm}$ $(10^5{\rm M}_\odot)$	$f_{\rm b}$
Aq-A-5	239.0	169.13	11.21	4.95	152.95	203822	152476	579342	5.03	26.40	0.55
Aq-B-5	183.0	75.93	4.08	4.88	66.97	108806	234310	444557	3.35	17.59	0.70
Aq-C-5	234.5	159.74	7.09	7.00	145.64	163726	273124	674547	4.11	21.59	0.51
Aq-D-5	240.2	171.67	7.59	12.10	151.97	159591	442966	657760	4.40	23.10	0.68
Aq-E-5	206.3	108.74	3.58	8.75	96.39	101041	431167	550757	3.33	17.50	0.67
Aq-F-5	209.0	113.05	8.65	8.86	95.51	331692	620784	791829	2.30	12.06	0.96
Aq-G-5	204.4	105.83	11.43	6.00	88.40	346061	328784	708979	2.83	14.88	1.03
Aq-H-5	183.1	76.06	2.95	5.01	68.10	91792	273228	525235	2.96	15.56	0.61
Aq-C-6	235.5	161.82	9.86	5.95	146.00	28702	26803	84525	32.90	172.73	0.57
Aq-C-4	234.4	159.48	8.39	5.31	145.71	1526514	1637981	5399079	0.51	2.70	0.49

Table 1. Primary numerical parameters of the simulated haloes at $z = 0$. We list the virial radius defined as a sphere enclosing an overdensity of 200 with respect to the critical density. The further columns give total mass, gas mass, stellar mass and dark matter particle mass inside the virial radius. The corresponding numbers of gaseous cells, star particles, and dark matter particles are given next, followed by the gas mass and dark matter resolutions in the high-resolution region. Finally, the last column gives the baryon fraction, $f_{\rm b} \equiv (\Omega_{\rm dm}/\Omega_{\rm b})(M_{\rm gas} + M_\star + M_{\rm bh})/M_{\rm dm}$ relative to the cosmological mean. In all the runs, the gravitational softening has been kept fixed in comoving units at $z \geq 1$ and in physical units (680 pc for level 5 runs) at $0 \leq z < 1$.

of our full simulation set[1]. The present-day virial masses[2] that we quote are for the evolved hydrodynamical haloes. Note that in a pure dark matter simulation, the corresponding masses will be slightly larger because the reduction of the baryon content below the universal mean through non-gravitational feedback slows the mass growth of the haloes. The baryon fraction $f_{\rm b}$ of our haloes relative to the cosmological mean is reduced typically by 30% at $z = 0$, with some systems having lost up to half their baryons (Aq-A and Aq-C), and others essentially none (Aq-F and Aq-G).

The original Aquarius initial conditions contained only dark matter particles. For our simulations, we add gas by splitting each dark matter particle into a pair of one dark matter and one gaseous cell, with their masses set according to the cosmological baryon mass fraction, and a separation equal to half the original mean interparticle spacing, keeping the centre of mass and centre-of-mass velocity of each pair fixed. In this way, two interleaved grids (or actually 'glasses', in the case of our high-resolution region) of dark matter particles and gaseous cells are formed. We note that we split *all* the particles, regardless of whether they are part of the high-resolution region or the surrounding low-resolution volume, such that the whole volume is filled with gas. There is hence no pressure discontinuity at the boundary of the high-resolution region. The evolved haloes at $z = 0$ show zero contamination of the virialized regions by low resolution dark matter particles, a tribute to the high quality of the initial conditions (which were created by Adrian Jenkins for the Aquarius project).

2.2 Simulation code

In the following, we briefly describe our simulation code and the most important parameter settings used in this work. In the interest of brevity, we only discuss the most important code characteristics and refer, for further details, to the code paper of AREPO (Springel 2010) and the application tests discussed in Vogelsberger et al. (2012) and Sijacki et al. (2012).

The moving-mesh code AREPO employs a dynamic Voronoi mesh for a finite-volume discretization of the Euler equations. The fluxes between the individual Voronoi cells are calculated using a second-order Godunov scheme together with an exact Riemann solver. This approach is akin to ordinary grid-based Eulerian schemes for hydrodynamics, except that an unstructured mesh is used that is generated as the Voronoi tessellation of a set of mesh-generating points. In addition, these mesh-generating points may be moved freely, inducing a dynamical and continuous transformation of the mesh without the occurrence of pathological mesh distortions. The most interesting way to exploit this freedom of a dynamic mesh is to move the mesh-generating points with the local flow velocity. In this default mode of operation, a pseudo-Lagrangian method results where the mass per cell is kept approximately constant and a Galilean-invariant numerical method is obtained.

The automatic adaptivity of AREPO is thus similar to that of SPH, but the mass per cell is not forced to stay strictly constant. Instead, local variations in the gas mass per cell may occur, but in case the mass deviates by more than a factor of 2 from the target gas mass resolution, we either split the cell into two, or dissolve it (as in Vogelsberger et al. 2012), which is very similar to a Lagrangian refinement criterion in adaptive mesh refinement (AMR) codes. But thanks to the adaptive nature of the dynamic mesh, such refinement and derefinement operations are needed much less frequently. Perhaps the most important advantage of AREPO compared to traditional mesh codes with a static mesh is a significant reduction of advection errors, which becomes particularly relevant for highly supersonic motions. Compared to SPH, the most important advantages are the absence of an artificial viscosity, a reduced sampling noise, a higher ac-

[1] Omitting the dark matter only simulations considered in section 5 for the sake of brevity.
[2] Following standard procedure, we define the virial mass as the mass contained within a sphere that encloses a mean matter density 200 times the critical density for closure, $\rho_{\rm crit} = 3H^2(z)/(8\pi G)$.

curacy of gradient estimates, and a faster convergence rate in multi-dimensional flow.

As far as the gravity solver and collisionless dynamics are concerned, AREPO applies the same techniques as the TreePM code GADGET (Springel 2005). This makes the two codes particularly well suited for a code comparison that focuses on an analysis of the differences induced by the hydrodynamic treatment alone, and/or differences due to feedback implementations, as differences originating in the treatment of gravity can be largely excluded. In previous work, we have carried out such comparisons (e.g. Scannapieco et al. 2012; Sijacki et al. 2012; Vogelsberger et al. 2012) for models with identical (minimal) feedback physics. The simulations presented in this paper use a new strong feedback model (see below) and can be directly compared with the GADGET results obtained by Scannapieco et al. (2009) and Aumer et al. (2013) for matching haloes from the Aquarius sample, as well as with the results reported in the Aquila project (Scannapieco et al. 2012) for a multitude of codes and feedback models applied to the Aq-C halo.

2.3 Physical model for galaxy formation

We here employ a novel implementation of the most important physical processes of galaxy formation in AREPO, presented in detail in Vogelsberger et al. (2013). For the sake of brevity, we list here only the most important characteristics and refer to the papers of Vogelsberger et al. (2013) and Torrey et al. (2013) for full details and cosmological tests. The model includes the following.

(i) Primordial and metal-line cooling with self-shielding corrections.

(ii) A simple subresolution model for the interstellar medium (ISM), which pictures the ISM as a two-phase medium that is predominantly composed of cold clouds embedded in a tenuous, supernova-heated phase (Springel & Hernquist 2003).

(iii) Stellar evolution, gas recycling and chemical enrichment. The chemical enrichment follows nine elements (H, He, C, N, O, Ne, Mg, Si and Fe) independently, and tracks the overall metallicity and the total mass return from stars to gas.

(iv) Stellar feedback realized through a kinetic wind scheme in which the wind velocity is scaled with the local halo size (similar to Puchwein & Springel 2013), which in turn is estimated by the dark matter velocity dispersion. The adopted scaling of the mass loading of winds corresponds to energy-driven winds.

(v) A metal loading of outflows that is determined independently of the mass loading of the winds. This is required to simultaneously reproduce the stellar mass content of low mass haloes and their gas oxygen abundances.

(vi) BH seeding, BH accretion and BH merging procedures based on an updated version of the model described in Springel et al. (2005a). The BH growth distinguishes between quasar- and radio-mode feedback. In addition, a novel prescription for radiative feedback from AGN is included that modifies the ionization state and hence the cooling rate nearby to an active BH. This implementation assumes an average spectral energy distribution and a luminosity-dependent scaling of obscuration effects.

(vii) A spatially uniform UV background following the model of Faucher-Giguère et al. (2009), which completes H I reionization at a redshift of $z \simeq 6$.

(viii) A new Lagrangian tracer particle formalism introduced by Genel et al. (2013) that follows the flow faithfully with a Monte Carlo-based approach.

We set the free parameters of the model to identical values (modulo a minor change, as described below) as identified by Vogelsberger et al. (2013) for their best match model in cosmological simulations of galaxy formation. These fiducial settings produce a good match to the stellar mass to halo mass function, the galaxy luminosity functions, the history of the cosmic star formation rate (SFR) density and to several other key observables. These parameters hence represent a good candidate for testing the model at higher resolution than possible in simulations of uniformly sampled cosmological volumes. We only deviate from Vogelsberger et al. (2013) with respect to two minor points. As their radio-mode AGN feedback in large haloes is based on the stochastic triggering of hot bubbles in halo atmospheres, numerical convergence with varying resolution can not necessarily be expected for individual objects, but only for the population mean. Because this could spoil our convergence study, we replaced the bubble heating with a much gentler halo heating model where more bubbles of individually much weaker strength are created. We note however that this feedback channel is almost unimportant for our galaxies because of their moderate halo mass. The other small change that we made concerns the galactic winds, which we opted to endow with some amount of thermal energy in order to make them 'hot' rather than 'cold' when they are launched. Our tests have shown that providing some amount of thermal energy to galactic winds makes the gas flows in the haloes smoother and more regular without changing the stellar mass of the galaxies in any significant way. In contrast, if the wind is ejected cold, we sometimes see cold string-like gas features in the circumgalactic medium, which appear to be an artefact of this wind model. To preclude the possibility of in situ star formation in these features, we adopted a modification of the wind model where the energy given to the wind is split into equal parts into thermal and kinetic form, instead of assigning it all as kinetic energy and leaving it fully up to the hydrodynamical interactions to dissipate it to heat. Since all the other wind parameters (in particular the wind velocity and the wind energy flux) are fixed as in Vogelsberger et al. (2013), this reduces the wind mass loading slightly because the wind now also carries away some energy in thermal form.

It is worthwhile to emphasize the relation of our simulations to the runs carried out for the Aq-C halo in the Aquila comparison project (Scannapieco et al. 2012). There, AREPO had been run without an explicit feedback model (except for the supernova feedback implicit in the ISM pressurization model), and without metal cooling. Interestingly, simulations with comparably weak feedback done with the RAMSES code cooled a very similar amount of gas as AREPO, which is a reassuring agreement and suggests that systematic differences between AMR and our moving-mesh technique are not significant for determining how much gas becomes available for star formation in the first place (we note that this does not preclude, however, that there are other systematic differences elsewhere). There has been no change in the ba-
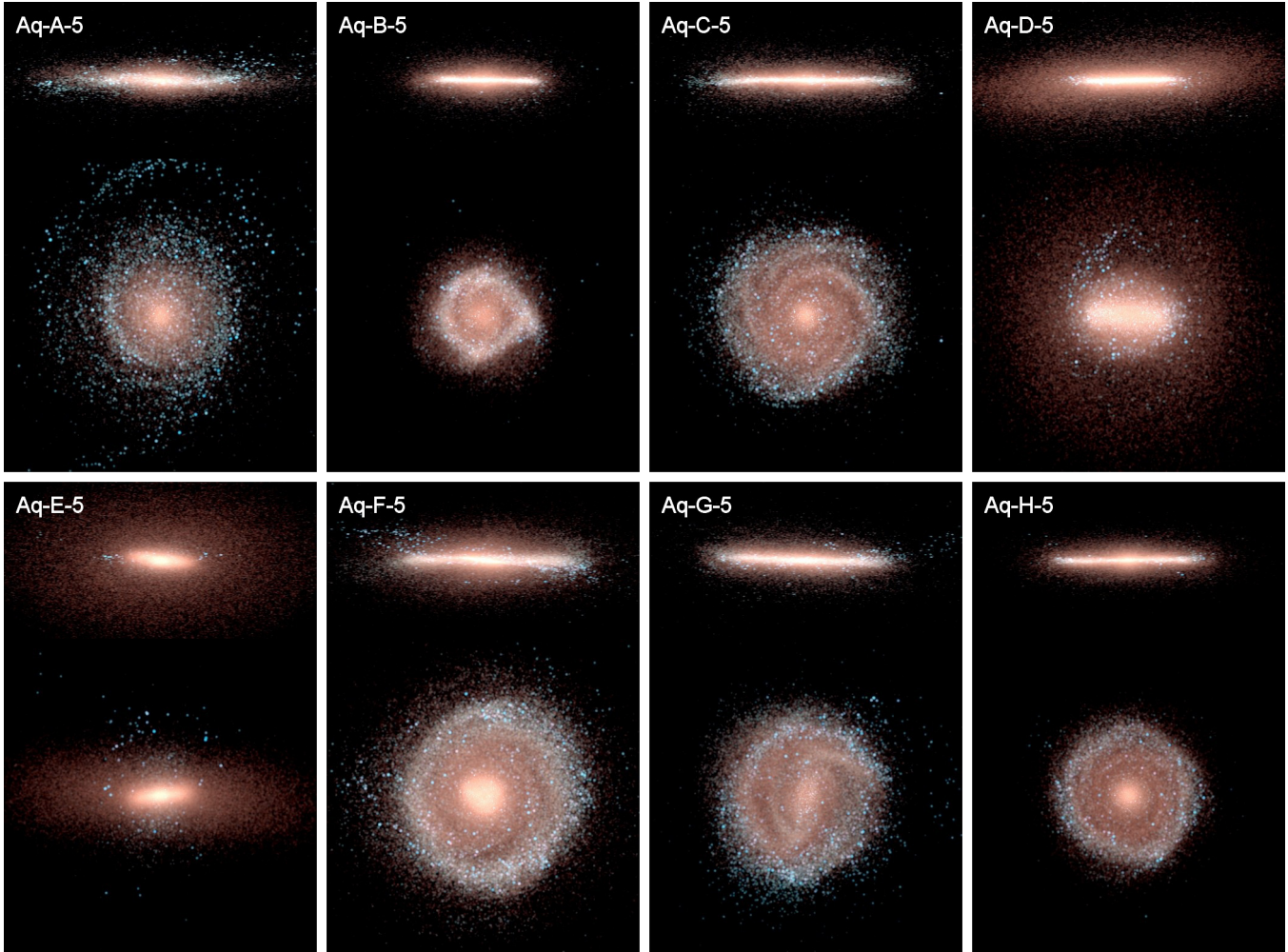
Figure 1. Projected stellar density for the eight simulated haloes at $z = 0$. The chosen projection box is 50 kpc in all directions and is centred on the halo potential minimum. Edge-on (top portion of each panel) and face-on views (bottom portion of each panel) are displayed. A stellar disc is detectable in all the simulated haloes. The images are obtained by logarithmically mapping the K-, B- and U-band luminosity of the stars to the red, green and blue colour channels in order to have a visual impression of the age of the different stellar populations contained in the final galaxy. As a result, very young stars show up blue while older stars appear progressively redder.

sic methods for calculating gravity and hydrodynamics in the AREPO code since the Aquila project; hence, the improvements in the results we report in this paper can be entirely attributed to the new physics models for star formation, BH growth and associated feedback channels that we adopt here. In particular, the key new process invoked in the present simulations is an explicit modelling of galactic winds, which is the primary process responsible for the differences with respect to the AREPO runs in the Aquila project. The winds curtail excessive high-redshift star formation, thereby reducing the size of the central spheroids while leaving enough gas around to form a rotationally supported disc at late times. This allows our new simulations to follow the path for successful disc formation identified in the Aquila project.

3   PRESENT DAY GALAXY STRUCTURE

3.1   Stellar discs

In Fig. 1, we show the stellar mass distributions of all of our eight simulated haloes at $z = 0$, both in face-on and edge-on projections. The images were constructed by mapping the K-, B- and U-band luminosities to the red, green and blue channels of a full colour composite image. Young stellar populations hence appear blue, old stellar components appear red. All images use the same logarithmic mapping of stellar luminosity to image intensity and display the same physical extension of 50 kpc on a side. The face-on orientation used for the projections was defined through the angular momentum of the cold galactic gas. Using instead the major axis of the moment-of-inertia tensor of the stars or the stellar angular momentum vector yields essentially the same directions, and represents an equally well working choice for these galaxies. For definiteness, we define an aligned coordinate system $(x'y'z')$ for each galaxy where the z'-axis points along the angular momentum of the cold gas, while the y'-
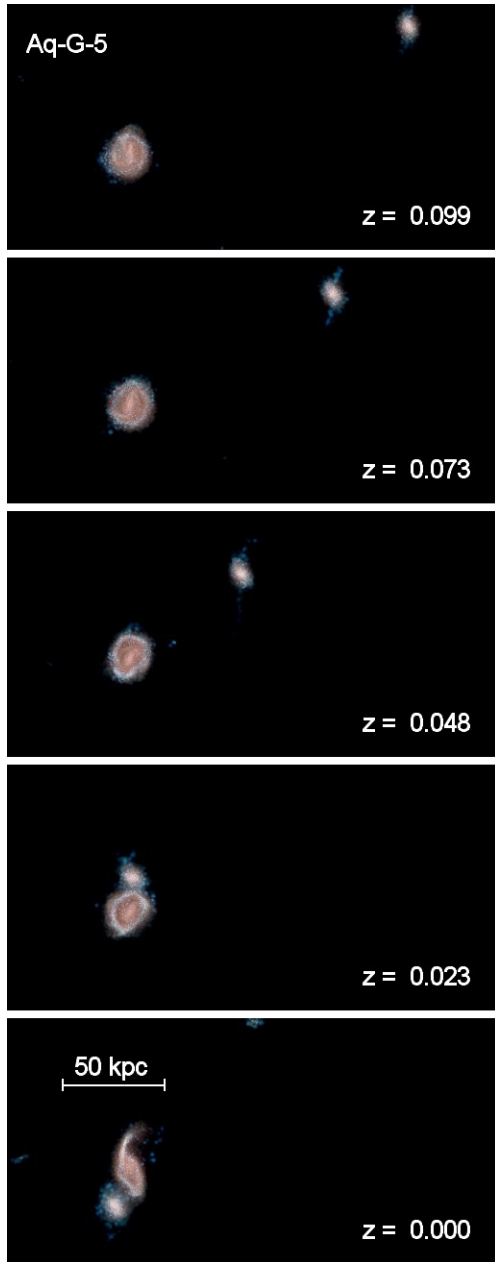
Figure 2. Time evolution of the Aq-G-5 simulation directly before $z = 0$.

axis points along the intersection of the $z' = 0$ plane with the $z = 0$ plane of the simulation's original coordinate system. This leaves two possible directions for the x'-axis: we pick the one with the smaller angle between the positive x' and x axes.

Clearly evident in Fig. 1 is the pronounced disc morphology of almost all of the systems. The one exception is the galaxy Aq-E-5, which is the reddest among the set. Most of its stars appear to lie in an elongated spheroid that shows substantially flattening. There is also a feeble disc of young stars misaligned with the old flattened stellar distribution. The disc of galaxy Aq-D-5 is dominated by a prominent bar, and also is comparatively red. The other six galaxies feature nicely symmetric, thin and extended discs, with some

indication of a red bulge in the centre, which is however not prominent enough to be readily apparent in the edge-on projections. Interestingly, these well-defined discs show blue outer rings and some spiral features that indicate substantial star formation in these regions. The blue/red appearance of the discs shows a qualitative resemblance with some observed galaxies, such as NGC 7217[3] which compares quite nicely with Aq-H-5, for example.

Actually, we have shown the galaxy Aq-G-5 at $z = 0.07$ rather than at $z = 0$ in Fig. 1. This is done because Aq-G-5 happens to just undergo an encounter with a massive satellite galaxy at $z = 0$, inducing a significant tidal perturbation that started to deform its disc and created a prominent tidal arm to the North. This is seen explicitly in Fig. 2, which displays snapshots of the time evolution of the Aq-G-5 system from $z = 0.1$ to 0. In order to avoid that our results are distorted by the strong encounter right at $z = 0$, we use the $z = 0.07$ output of Aq-G-5 for all subsequent analysis.

In Fig. 3, we show azimuthally averaged face-on stellar surface density profiles of our eight galaxies (black circles). The profiles are obtained by projecting on the $x'y'$ plane (see above) the mass of all stellar particles contained in a box centred on the halo potential minimum, with a total height equal to $0.1 \times R_{\rm vir}$. Stars are binned in circular annuli in the projection plane, and the total stellar mass of each bin is then divided by its surface area to get the surface density.

Interestingly, most of the galaxies show surface density profiles that present, in their outer parts, the characteristic exponentially declining trend observed in many spiral galaxies. In some of the simulated galaxies a clear central excess can be seen, signifying the presence of a central bulge. To quantify the importance of the two contributions we have carried out two-component fits of the surface density profiles with a Sérsic (1963) profile (red lines) for the central part, and an exponential profile (blue lines) for the outer parts. The fits are performed by simultaneously varying the parameters of the exponential and Sérsic profiles. Finding first the optimal parameters of the exponential profile and subsequently modelling the central residual excess with the Sérsic profile, as done in Scannapieco et al. (2011), does not lead to significant differences in the results. The best-fitting parameters are listed in Table 2.

We find that these fits work quite well in most of the cases, and hence yield a tentative estimate of the bulge and disc stellar masses, and of the disc-to-total (D/T) ratio. These quantities are also reported in Table 2. We note however that such profile fits, which form the basis of photometric determinations of the bulge-to-disc ratio, are often not sufficiently unique to allow a robust decomposition. In particular, fits with very similar quality parameter Q can be obtained for quite different values of $r_{\rm cut}$, and sometimes this affects the structural parameters of the disc and bulge strongly even though the total recovered profile does not show any appreciable difference. This technique is also known to typically overestimate the D/B mass ratio. The essentially *pure discs* we obtain for Aq-B, Aq-C and Aq-G therefore need to be taken with a grain of salt.

This is corroborated by a much more reliable kinematic bulge-to-disc decomposition which we consider in Fig. 4.

---

[3] see e.g. http://skycenter.arizona.edu/gallery/Galaxies/NGC7217
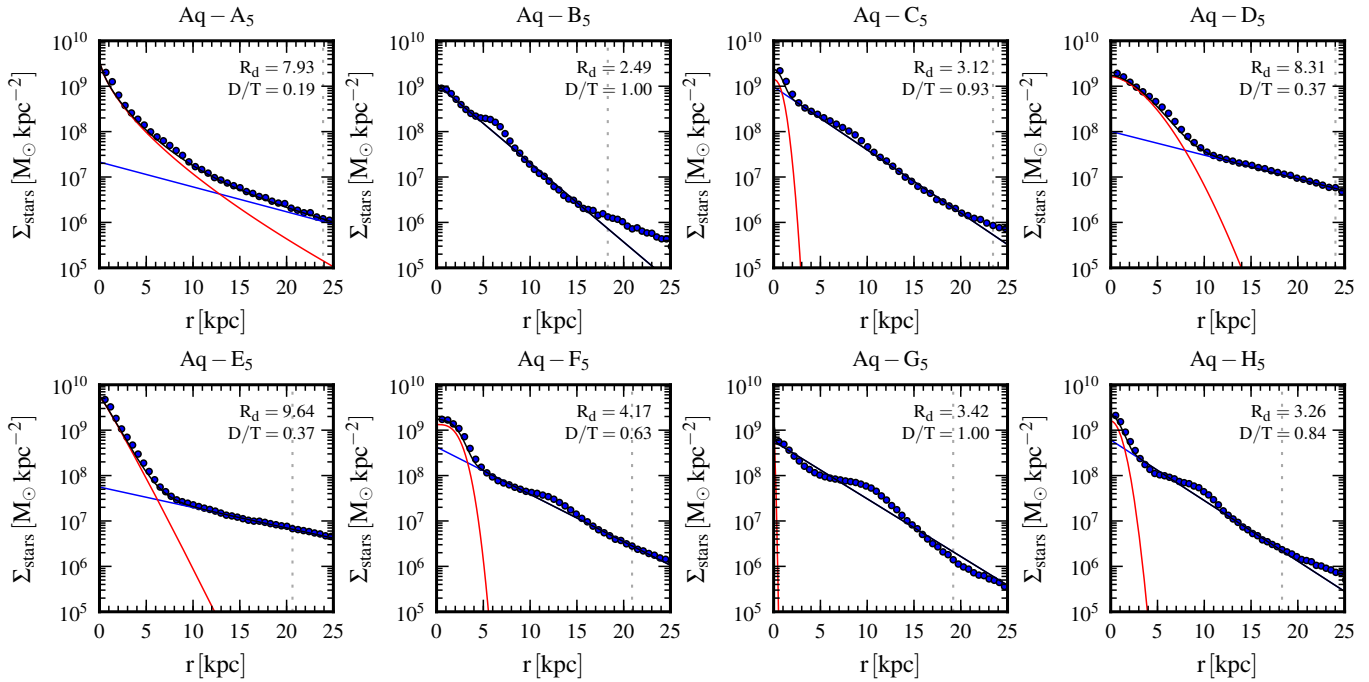
Figure 3. Stellar surface density profiles of the simulated galaxies, seen face-on. Decompositions of the total profile into an exponential disc and a Sérsic profile are also shown (provided the Sérsic fit is sufficiently well defined). The fits are carried out up to the vertical dotted line located at $0.1 \times R_{\rm vir}$. The resulting disc scalelength and D/T mass ratio are indicated in each panel. A comprehensive list of the structural parameters derived from the disc-bulge decomposition can be found in Table 2.

Run	$\log_{10} \Sigma_{\rm d}$ $(M_\odot {\rm kpc}^{-2})$	$R_{\rm d}$ (kpc)	$\log_{10} \Sigma_{\rm eff}$ $(M_\odot {\rm kpc}^{-2})$	$r_{\rm eff}$ (kpc)	n	Disc mass $(10^{10} M_\odot)$	Bulge mass $(10^{10} M_\odot)$	D/T	Total mass $(10^{10} M_\odot)$	Fit Mass $(10^{10} M_\odot)$
Aq-A-5	7.329	7.929	6.831	3.148	1.551	0.843	3.632	0.19	4.363	4.475
Aq-B-5	9.052	2.493	7.614	0.021	0.693	4.399	$< 10^{-4}$	1.00	4.691	4.399
Aq-C-5	8.988	3.124	8.560	0.835	0.446	5.961	0.474	0.93	6.617	6.435
Aq-D-5	8.004	8.306	8.339	3.353	0.593	4.379	7.391	0.37	10.78	11.77
Aq-E-5	7.747	9.641	8.204	1.971	0.939	3.264	5.484	0.37	7.919	8.748
Aq-F-5	8.628	4.170	8.765	1.924	0.323	4.637	2.697	0.63	7.256	7.334
Aq-G-5	8.758	3.420	8.013	0.120	0.664	4.207	0.006	1.00	4.229	4.213
Aq-H-5	8.784	3.255	8.500	1.046	0.504	4.045	0.784	0.84	4.865	4.830

Table 2. Parameters of the surface density profile decomposition. For each run the columns give (from left to right): the logarithm of the central surface density of the disc, the disc scale-length, the logarithm of the bulge surface density at the effective radius, the bulge effective radius (defined as the radius enclosing half of the bulge mass), the Sérsic index of the bulge, the inferred disc mass, the inferred bulge mass, the D/T mass ratio, the total mass of the system as computed by the simulation output and the total mass of the system as derived from the fit.

Here we follow Abadi et al. (2003) and define for every star with specific angular moment J_z around the symmetry axis a circularity parameter

$$\epsilon = \frac{J_z}{J(E)}, \qquad (1)$$

where $J(E)$ is the maximum specific angular momentum possible at the specific binding energy E of the star. We note that another definition of circularity that is sometimes used in the literature (e.g. Scannapieco et al. 2009, 2012) is to replace $J(E)$ with the angular momentum $r\,v_c(r)$ of a star in circular motion at the star radial distance r, where $v_c(r) = \sqrt{GM(<r)/r}$ is the circular velocity, yielding

$$\epsilon_V = \frac{J_z}{r v_c(r)}. \qquad (2)$$

To allow an easy comparison with both literature conventions, we include results for both definitions in our mass-weighted circularity distributions $f(\epsilon)$. We note that the distributions presented in Fig. 4 are normalized such that $\int f(\epsilon)\,{\rm d}\epsilon = 1$.

Perfectly cold stellar discs should show up as a narrow distribution around $\epsilon \sim 1$. As we see from Fig. 4, there are massive discs in all of our systems, but with varying contributions to the total stellar mass. The best characterized disc – considering both the prominence of the peak at $\epsilon \sim 1$ and the resulting mass fraction – is actually found in halo Aq-C, consistently with the original motivation for picking this halo for the Aquila comparison project, which was simply the desire to select a system that is most likely to make a disc. This has, among other factors, to do with the quiet for-
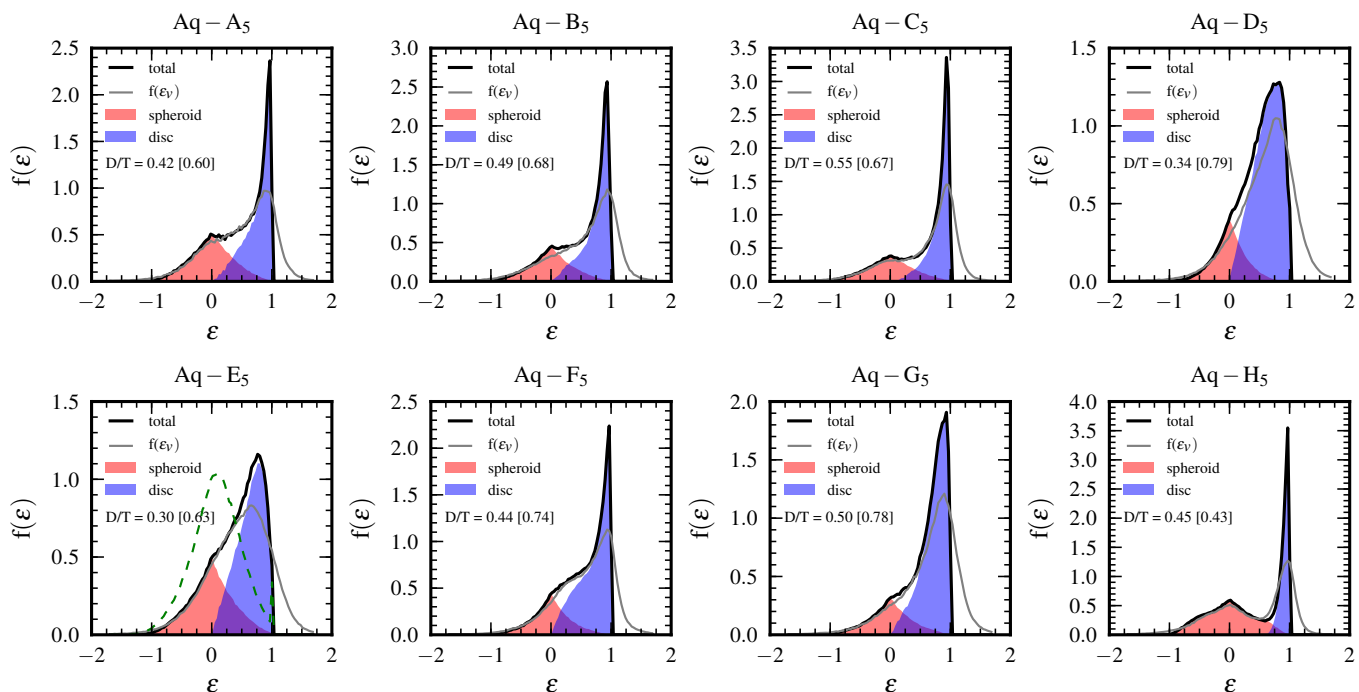
Figure 4. Distribution of the mass-weighted stellar circularities ϵ for the eight Aquarius haloes at $z = 0$. The plots are obtained by considering only stars with $r < 0.1\,R_{\rm vir}$. The solid black lines show the ϵ distributions obtained by following the definition of Abadi et al. (2003). The distributions are further subdivided into a bulge (red) and a disc (blue) component by mirroring around zero the fraction of stars with negative ϵ and considering the resulting distribution as making up the bulge. The D/T mass ratios derived from this kinematic decomposition are reported in the legend of each panel in square brackets, while the other values are obtained from the fraction of stars with $\epsilon > 0.7$. The thin grey lines show the distribution of stellar circularities if the definition of ϵ_V adopted in the Aquila project is used. For the Aq-E-5 system, an additional dashed line is shown that gives the distribution of ϵ if the face-on projection is aligned with the disc of young stars forming in this system, which is roughly perpendicular to the rotation direction of the old stars.

mation history of Aq-C. Its halo forms comparatively early for systems of this mass (Boylan-Kolchin et al. 2010), thus favouring the unperturbed growth of a nice disc over an extended period of time.

The D/T ratios obtained from the kinematic decomposition are included in the individual panels of Fig. 4, based on the fraction of stars with $\epsilon > 0.7$ (Aumer et al. 2013, find this measure to be roughly equivalent to the fraction $\epsilon_V > 0.8$). Yet another kinematic measure of the disc fraction is based on the original approach of Abadi et al. (2003), who defined as bulge component twice the fraction of stars with $\epsilon < 0$. This gives the highest kinematic estimates of D/T ratios for the systems and can be seen as a plausible upper limit on the disc fraction. We also include these values in square brackets in the individual panels of Fig. 4. The highest D/T ratios we obtain are about ~ 0.5 based on the $\epsilon > 0.7$ definition, and even reaching up to 0.8 when the measure of Abadi et al. (2003) is adopted. Our discs are equally prominent as the best cases in Aumer et al. (2013), but not significantly stronger. They are better defined and feature a higher D/B ratio than most of the other successful disc formations in the recent literature, which were in part reporting D/T values based on photometric decompositions. Note that with the latter method, we would conclude to have obtained pure discs in some of the systems.

In Fig. 5, we compare the scalelength of our exponential discs, as measured from fits to the surface brightness profiles, with observational data of the size-luminosity rela-

tionship in the B band. The observational data were taken from the compilation of literature catalogues[4] considered in Graham & Worley (2008), and have been corrected for inclination and (internal) dust extinction effects by adopting the prescription described in section 2.2 of their work. We also report their best-fitting relation (solid black line) and the observed upper boundary to the disc surface brightnesses (dotted black line). We remind that since the disc scalelenghts of the simulated galaxies were derived from face-on surface brightness decompositions, no correction for inclination is required in this case and dust extinction is neglected for the determination of the B-band luminosities. All the simulated galaxies have realistic B-band magnitudes that lie below the (observed) upper boundary to the surface brightness. It is also interesting to note how the simulated systems with a substantial bulge (Aq-A, Aq-D and Aq-E) are preferentially located towards larger discs scale-lenghts with Aq-E also featuring a substantially lower B-band luminosity, although within the observed scatter of the data, with respect to the best-fitting relation. Another simple measure of the galaxy size is obtained by considering the stellar half-light Petrosian radii in the r band $R_{\rm r,50}$. This can be compared with observational data for the $R_{\rm r,50} - M_{\rm r}$ relationship, which is done
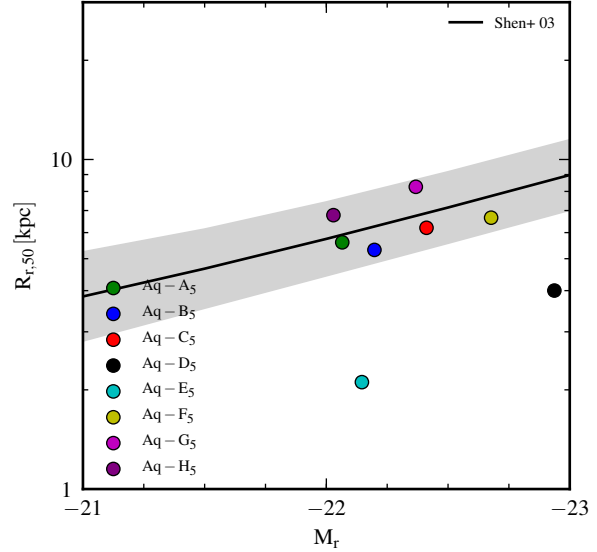
---

[4] The references to the catalogues, also given in the legend of Fig. 5, are: Möllenhoff (2004); MacArthur et al. (2003); Graham (2001, 2002).
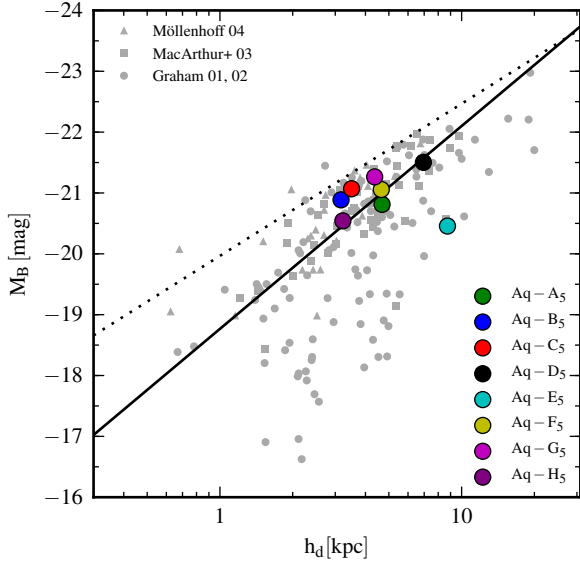
Figure 5. *B*-band luminosity versus disc scale-length for the eight simulated haloes (coloured circles) compared with the compilation of data sets (grey symbols) considered in Graham & Worley (2008). The disc scale-lengths of the simulations come from fits to the surface brightness profiles, and for the determination of the *B*-band luminosity no dust attenuation was taken into account. Data points are corrected for inclination and dust effects as in Graham & Worley (2008). From the same reference we also plot the best-fitting relation (solid line) and the observed upper boundary to the surface brightness (dotted line).

Figure 6. Stellar half-light Petrosian radius versus Petrosian absolute magnitude in the r band for our simulated galaxies at $z = 0$, compared with the median observed relation by Shen et al. (2003) for late-type galaxies in the SDSS. The shaded region represents the observed 1σ dispersion around the median value.

in Fig. 6. We find that the simulated galaxies fall right into the observational distribution of half-light radii at comparable stellar luminosities found by Shen et al. (2003) for the Sloan Digital Sky Survey (SDSS), the most notable exceptions being the Aq-D and Aq-E haloes that produce galaxies that are too compact given their luminosity. We hence conclude that our galaxies have sizes for their luminosities that agree well with the observational data.

Another important property of stellar discs is their vertical structure. Numerical simulations of galaxy formation often find it difficult to reproduce the cold (i.e. low velocity dispersion) and thin stellar disc structures (typical scaleheight $\sim 100 - 200$ pc) observed in late-type spirals and in the Milky Way (e.g. Stinson et al. 2013b). While this may partially reflect a lack of resolution needed to correctly capture the vertical dynamics of the simulated discs – we remind that even in the case of Aq-C-4, our highest resolution simulation, the gravitational softening is 340 pc – the treatment of the galaxy's ISM and stellar feedback plays an even more important role. In the present simulations, stars are born within a gaseous disc approximately in vertical hydrostatic equilibrium, where the gas pressure gradient balances the vertical gravitational field. The thickness of this gaseous structure is thus set by the sound speed of the star-forming phase, which should be low enough such that the scaleheight of the gaseous disc is comparable with that of the thin stellar disc. This could represent a potential problem for the Springel & Hernquist (2003) ISM model adopted in this work, because the effective sound speed needed to sta-

bilize the gaseous disc against fragmentation is larger than that expected for a stellar disc with ~ 100 pc thickness.

In Fig. 7, we present the mass-weighted vertical velocity dispersion (upper panels) and the mass-weighted second moment of the *z*-coordinate (a measure of the disc scaleheight, lower panels) as a function of galactocentric radius of disc stars (i.e. stars with circularity parameter $\epsilon > 0.7$) for a subset of the simulated haloes hosting prominent discs. We display these quantities for three different age cuts: 'young' stars with age < 1 Gyr, 'old' stars with 1 Gyr < age < 5 Gyr, and the total sample of stars. The vertical velocity dispersion lies between 20 and 60 km s^{-1}, with a rapid increase in the innermost kpc and subsequently with a rather flat trend as a function of radius. These flat profiles imply strongly flared discs, with scaleheights rapidly increasing from ~ 100 pc to a few kpc in the outer regions. There is an apparent trend of both velocity dispersion and scaleheight with stellar age in the sense that young stars have preferentially a lower velocity dispersion and hence a smaller scaleheight compared to old stars. Overall, the scaleheight of the simulated discs are too large with a typical average value of ~ 0.5 kpc within a radius of 10 kpc. This excessive thickness of the simulated discs is most likely due to our ISM treatment, although the trend with stellar age suggests that at least part of it might have a different origin, for example disc heating by satellites.

In Fig. 8, we consider the Tully-Fisher relation (Tully & Fisher 1977) of the simulated galaxies at $z = 0$. We determine the stellar masses associated with each galaxy by simply summing the masses of the stellar particles that lie within 10% of the virial radius of each halo (the centre of the halo coincides with the position of its potential minimum), while for the rotation velocity we take the circular velocity defined as $v_c(r) = \sqrt{GM(<r)/r}$, where $M(<r)$ is the enclosed total mass at the radius r. Different choices for
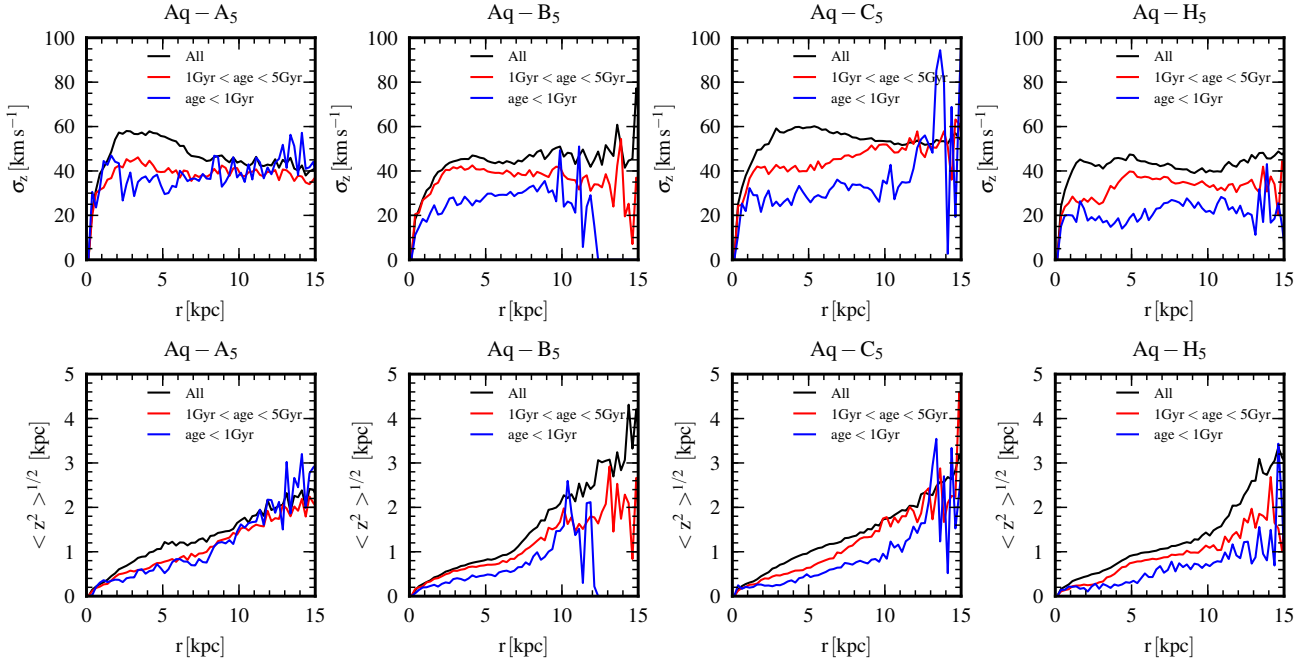
Figure 7. Vertical velocity dispersion (upper panels) and scaleheight (lower panels), computed as the mass-weighted second moment of the z-coordinate, of disc stars as a function of galactocentric radius for a subset of the simulated haloes hosting prominent disc components. Disc stars are selected as stars with circularity parameters $\epsilon > 0.7$ and the plots show the above quantities for three different age cuts: 'young' stars (blue lines), 'old' stars (red lines) and the total sample of disc stars (black lines). Young stars tend to be preferentially colder and hence feature a thinner vertical distribution with respect to old stars, but the typical disc scaleheights estimated from this analysis (~ 0.5 kpc) are too large when compared to observational data.
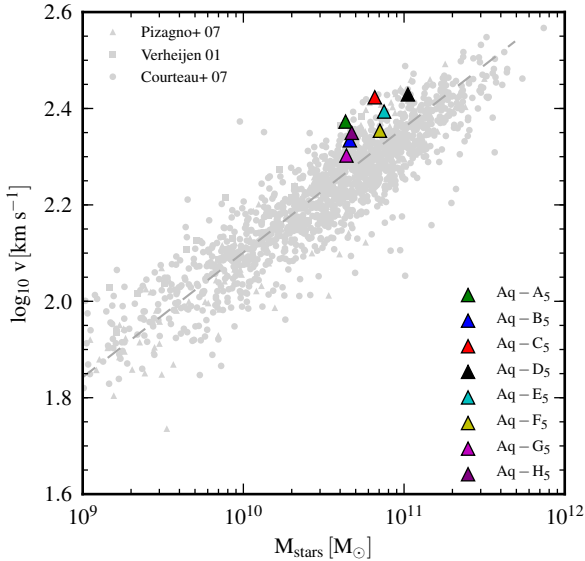
Figure 8. The Tully-Fisher relation for the simulated haloes at $z = 0$. Grey symbols represent the observational data sets given in the figure legend, while the long dashed line is the best-fitting relation derived from the same set of observations by Dutton et al. (2011). Triangular symbols show our simulation results. All the simulated galaxies fall comfortably within the observed scatter of the relation.

the radius at which v_c is measured and adopted as characteristic galaxy velocity are possible, and depending on the detailed shape of $v_c(r)$ (see Fig. 19 and Section 5.1 for a more detailed discussion of the rotation curves of the simulated galaxies) somewhat different values of the rotation velocity can be assigned to each galaxy. In what follows, we use for the Tully-Fisher relation the rotation velocity at $R_{\star,80}$, corresponding to the radius within which 80% of the stellar mass is enclosed. At that position the circular velocity of the galaxy has already reached the flat part of the rotation curve. We have investigated the range of systematic uncertainty in assigning a circular velocity to each galaxy by also considering the peak value of the rotation curves, finding no dramatic difference, except for the Aq-E halo, which in this case is pushed slightly above the scatter of the observed Tully-Fisher relation.

In Fig. 8 we include, as grey symbols, a collection of observed galaxies (from Verheijen 2001; Courteau et al. 2007; Pizagno et al. 2007) for which surface photometry and measurements of rotation velocities were available in the literature. This data set was already analysed by Dutton et al. (2011) and we follow their method to convert galaxy luminosities into (MPA/JHU group) stellar masses, with the appropriate normalization for a Chabrier (2003) initial mass function. The included best fit to the Tully-Fisher relation (long dashed line) is also taken from Dutton et al. (2011). Our simulated galaxies are close to the predictions of this best-fitting relation, and even the two cases that are located furthest away (haloes Aq-A and Aq-C) are comfortably within the observed scatter. However, the simulations are not evenly distributed around the best-fitting line, rather

they tend to lie preferentially above the observed relation, with none of the simulated points falling below. This may indicate still slightly too concentrated galaxies, or could in part reflect a selection bias in our sample. None the less, the comparison is encouraging and shows the ability of our cosmological AREPO simulations to form extended disc galaxies with the correct rotational speed.

A more careful comparison with the observed Tully-Fisher relation would require us to consider the actual kinematics of the gaseous and/or stellar components taken at some characteristic radius, usually 2.2 times the disc scale-length in some photometric band. Although this is in principle certainly feasible, we would like to note that for the scope of this work we are not interested in reproducing this relation in exquisite detail (which would also need a larger galaxy sample), but only in showing that our simulation methodology is able to produce realistic discs with reasonable rotation speed. We also note that if one examines the kinematic state of the gaseous and stellar components (see Figs. 19 and 20) more closely, the actual rotation velocities show only a slight deviation from the theoretical values adopted in the previous analysis. The deviation is usually towards lower velocities and this would improve the overall agreement between our simulated set of galaxies and the observations.

3.2   Gaseous discs

In Figs. 9 and 10, we show projections of the gas density and gas velocity fields for all eight simulated galaxies at $z = 0$. For each galaxy, three panels arranged in one row are shown, corresponding to a face-on and two edge-on projections along the principal directions defined for the $(x'y'z')$ frame of each galaxy. In each case, the projections show all the gas in a $50 \times 50 \times 10$ kpc box around a galaxy's centre. To enhance the visibility of the dense gas, the projections are weighted by the local gas density of each cell. The colour map encodes the gas density as image brightness, and the average gas temperature as colour hue. In addition, velocity field vectors are overplotted on a uniform grid of dimension 32×32. The length of the velocity vectors is proportional to the magnitude of the velocity in the projection plane, and either a blue or yellow colour is used for the arrows depending on the local temperature in order to enhance visual clarity.

The gas velocity fields in the face-on projections show a high degree of regular circular motions, especially in the dense neutral gas phase, which in the denser parts coincides with the star-forming regions. The surface density profiles of the gas are nearly flat, similar to the RAMSES simulations of Agertz et al. (2011). In a few cases, one also sees distortions of the gas disc, as expected based on the stellar distributions. For example, Aq-D-5 shows a bar-like gas distribution and a central density depression that is presumably related to AGN feedback. The lowest gas surface density is seen in Aq-E-5, which appears red in the stellar projections. Apparently, comparatively little star formation is ongoing in this system, but this is still occurring in a disc-like configuration, which is however roughly orthogonally oriented compared to the spin of the old stars. The morphology of the gas discs is quite smooth – a result primarily due to the fact that large density fluctuations in the gaseous disc are prevented by the effective equation of state used in the treatment of

the ISM – in stark contrast to the flocculent gas structures in the SPH simulations of Guedes et al. (2011) and Aumer et al. (2013), that are a consequence of their delayed cooling and/or early stellar feedback models.

Of particular interest in the gas projections are the edge-on views, which reveal the presence of low-density winds emanating from the star-forming discs. These outflows are a direct consequence of the strong kinetic wind feedback realized in our models. Gas streams on to the discs mostly at large radii and from directions close to the disc plane. However, there are also fountain-like inflows of dense gas scattered over the disc plane. The gas flow in the circumgalactic medium is clearly quite complicated, reflecting the expected complex interactions between the galactic winds, the gaseous halo and cosmological infall. We note that there is no evidence for a population of small dense gaseous 'blobs' in the halo as seen in many SPH calculations (Kaufmann et al. 2006; Guedes et al. 2011).

In Fig. 11, we compare the gas fractions of the simulated galaxies at the present day relative to observational data in the $f_{\rm gas} - M_{\rm R}$ plane. The gas fractions are defined as

$$f_{\rm gas} = \frac{M_{\rm gas}}{M_{\rm gas} + M_{\rm stars}}, \tag{3}$$

where $M_{\rm stars}$ and $M_{\rm gas}$ are the stellar and the gas mass within a radius $r = 0.1 \times R_{\rm vir}$. Stellar R-band magnitudes follow from the total stellar luminosity within the same radius in that passband[5]. For the gas, we use two different selection criteria: in one case, we measure the total gas fraction (circles) obtained by taking all the gas contained within the adopted radial cut, whilst in the second (triangles) only star-forming gas, again inside $r = 0.1 \times R_{\rm vir}$, is considered. Again, dust attenuation has not been taken into account. Data points in Fig. 11 have been obtained by cross-correlating two samples of nearby galaxies from Haynes et al. (1999b,a) presenting 21 cm H I observations and I-band photometry, respectively. H I integrated line fluxes are converted into gas masses through the formula (see e.g. Wakker & van Woerden 1991)

$$M_{\rm H\,I} = 2.35 \times 10^6 \left(\frac{D}{\rm Mpc}\right)^2 \left(\frac{S}{\rm Jy\,km\,s^{-1}}\right)\,{\rm M}_\odot, \tag{4}$$

where D is the distance to the galaxy and S the integrated H I line flux. The resulting masses are then multiplied by a factor of 1.37 to correct for helium abundance. I-band magnitudes are transformed to R band by assuming an average $(R-I)$ colour of 0.5 as in the original paper by Haynes et al. (1999a). They are also used as an input to compute the observed stellar masses through a linear fit of the simulation results in the $M_{\rm star} - M_{\rm R}$ plane. The total gas fractions that we measure for the simulations are between 10 and 30%, which is reassuringly high and consistent with the observational data. Strong feedback models often tend to have significant difficulties in retaining a sufficiently large amount of gas available for star formation at late times. Our models do not appear to suffer from this problem as can readily be seen

---

[5] Actually, in the current implementation of the stellar photometry R-band magnitudes are not available. To compute them we converted SDSS r-band magnitudes by using eq. A8 in Windhorst et al. (1991).
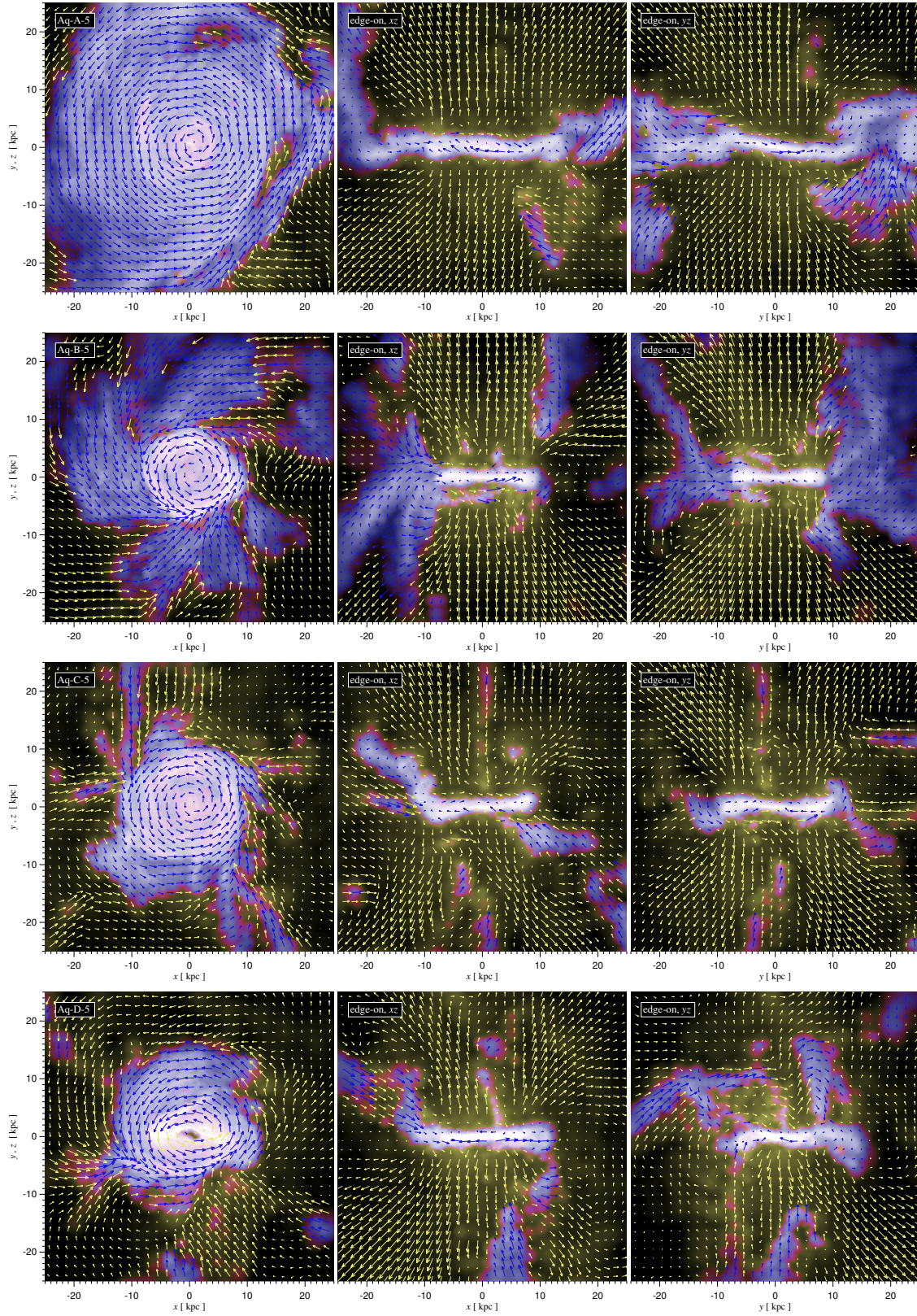
Figure 9. Gas distributions at $z = 0$ for the galaxies in haloes Aq-A to Aq-D. Each row of panels shows a face-on (left) and two edge-on (centre and right) views of the projected gas density for the resolution level 5. The chosen projection box is 50 kpc on a side and extends for a total of 10 kpc in the projection direction, centred on the halo potential minimum. The density-weighted gas velocity field is overplotted on the density distribution as arrows with lengths proportional to the gas velocity. The colour hue encodes the density-weighted gas temperature, ranging from blue (cold) to yellow (hot). The velocity vectors are drawn either in blue or yellow according to the local temperature in order to improve visibility. An extended gaseous disc supported by rotation is clearly visible in all cases, and in the edge-on panels, a global outflow motion of low-density gas, due to our kinetic wind feedback, can be seen.
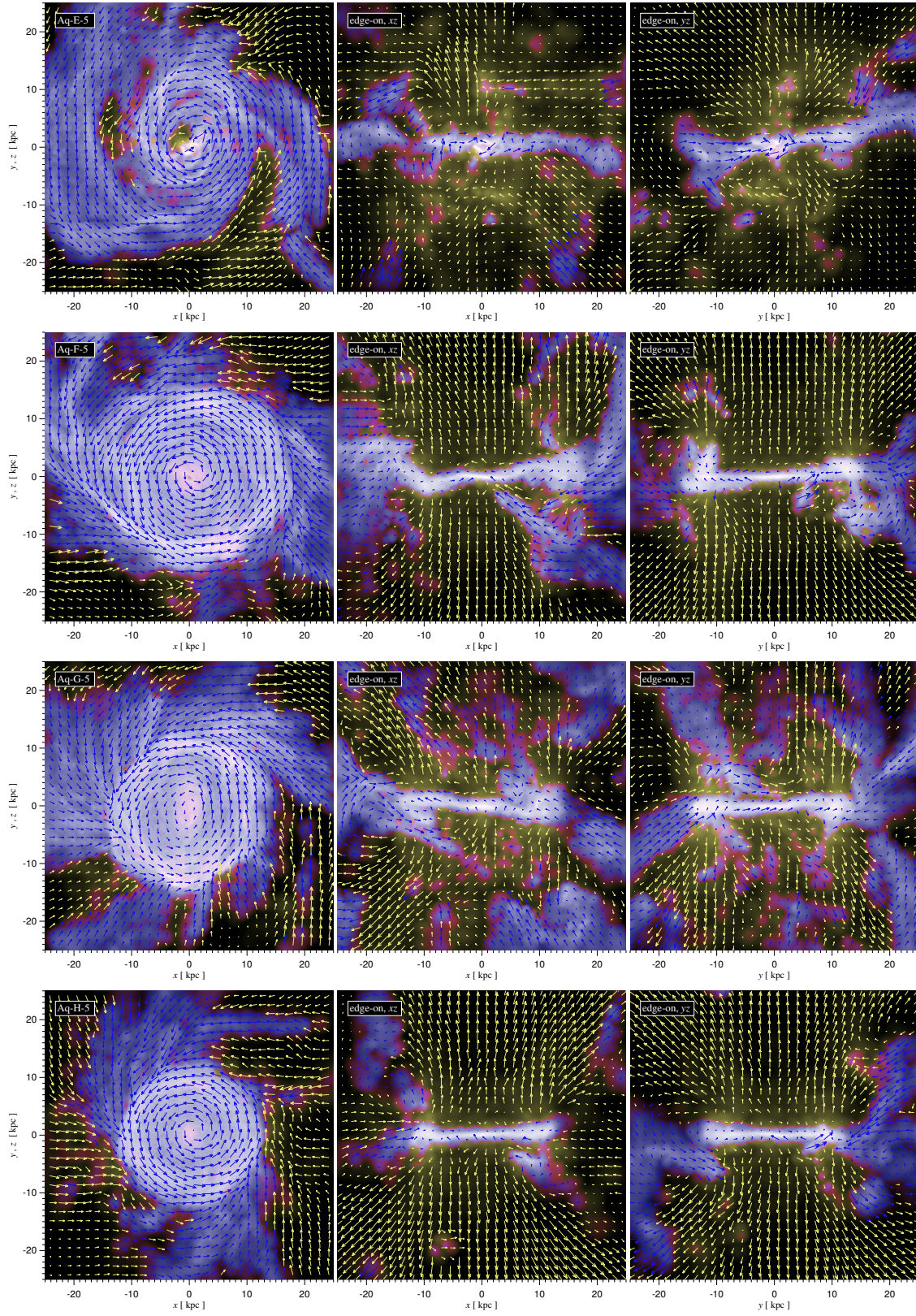
Figure 10. The same as Fig. 9, but for haloes Aq-E to Aq-H.
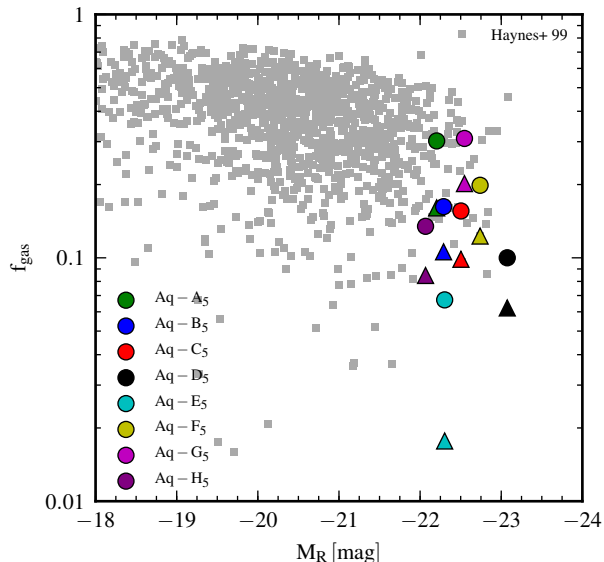
Figure 11. Gas mass fraction versus R-band magnitude for the eight simulated haloes (coloured symbols). The gas fractions were computed by considering all the baryons within $0.1 \times R_{\rm vir}$ (circles) or only the star-forming gas within the same radius (triangles). We compare the outcome of the simulations with a catalogue of galaxies compiled by Haynes et al. (1999b,a), for H I and optical observations, respectively. The observed gas fractions have been corrected for He abundance.

from the gas fractions of the star-forming phase, which are approximately a factor of 2 smaller than the total gas fractions but still sufficiently high to allow star formation to be active at $z = 0$. The only exception is the Aq-E halo, which has a gas fraction of $\sim 5\%$ ($\sim 2\%$ if only star-forming gas is taken into account). However, this system represents a particular case which is characterized by a rather strong merger event at $z \sim 1$. This triggered significant BH growth and associated feedback in our simulation, similar to the scenario of merger-induced formation of red ellipticals described in Springel et al. (2005c).

4   FORMATION HISTORY

A first qualitative impression of the formation history of our Milky Way-sized galaxies can be obtained from time evolution sequences of the stellar distributions of the simulations. In Figs. 12 and 13, we show this for Aq-C-5 and Aq-D-5 in an exemplary fashion. We have selected Aq-C-5 as a prototypical case making a nice disc at $z = 0$ (and because it is of particular interest due to its prior analysis in the Aquila project), and Aq-D-5 to show a partially failed disc, in this case through the formation of a strong bar. All the panels of the evolutionary sequence show the stars in a region of fixed physical size (50 kpc on a side centred on the galaxy's most massive progenitor), so that the images directly reflect the size evolution. The stars are shown with their luminosities in the rest frame, with the same mapping to colour and intensity as in Fig. 1. This mapping is kept the same at all redshifts and output times, so that the brightness and colour evolution of the images indicates the variations in the star

formation histories (SFHs) of the galaxies displayed at the individual redshifts. In particular, we can directly infer from the images that the heyday of blue disc formation lies in the redshift range $z \sim 0.5 - 1.5$ for our simulations. At higher redshift, the galaxies in our sample tend to be small and blue, whereas they redden progressively towards lower redshifts.

4.1   Star formation history

The realistic gas fractions measured for our galaxies at the present epoch support SFRs comparable to expectations for late-type galaxies at $z = 0$. This is seen in Fig. 14, where we compare the present-day SFRs of our simulations with observational data as a function of stellar mass. We measure the SFR time averaged over the past 0.5 Gyr by determining the stellar mass younger than 0.5 Gyr in a sphere of radius $0.1 \times R_{\rm vir}$ centred on the halo's potential minimum. For measuring the total stellar mass no age cut is applied. Note that this is the same procedure as adopted in the Aquila comparison project (Scannapieco et al. 2012). The background dots in Fig. 14 are a random subsample of nearby ($z < 0.1$) galaxies from the SDSS MPA-JHU DR7 data release 7 (DR7)[6], divided into the so-called 'blue cloud' and 'red sequence' on the basis of the colour condition (see again Scannapieco et al. 2012)

$$(g - r) = 0.59 + 0.052 \log \left(\frac{M_{\rm star}}{10^{10} M_\odot} \right), \qquad (5)$$

with the galaxy symbols coloured accordingly. Only 10% of the total sample is plotted. All the simulated galaxies are actively star-forming and tend to cluster around the current location of the Milky Way in the blue cloud, which is marked by the down-pointing triangle, with properties taken from Leitner & Kravtsov (2011, table 2). Again, a clear outlier in our galaxy set is the Aq-E halo, which is located in the outskirts of the red sequence. This is not surprising: given the small amount of gas left in the galaxy (see Fig. 11) a low SFR is expected. We also include in Fig. 14 the results of the Aquila comparison project at resolution level 5, for *all* the employed codes and feedback models (grey boxes). Interestingly, these simulations appear to systematically miss the location of the Milky Way and cluster around the dashed line. Those simulations that manage to reduce the SFR sufficiently end up being too red, while those with enough current star formation are too massive. This highlights the difficulty to arrive at simulation models that suppress star formation strongly especially at high redshift, but allow a high SFR at low redshift. Our new code combined with the implemented feedback physics achieves this considerably better than the models studied in the Aquila project.

In Fig. 15, we show plots of the formation history of the stars contained in each galaxy. This is based on the age histogram of stars that end up in the galaxies at the present time (again selected as all the stellar particles in a sphere of radius $0.1 \times R_{\rm vir}$ centred on the halo potential minimum). SFRs are then computed by dividing the stellar mass in each age bin by the width of the bin itself, so that they effectively represent the average SFR over the temporal bin

---

[6] http://www.mpa-garching.mpg.de/SDSS/DR7/
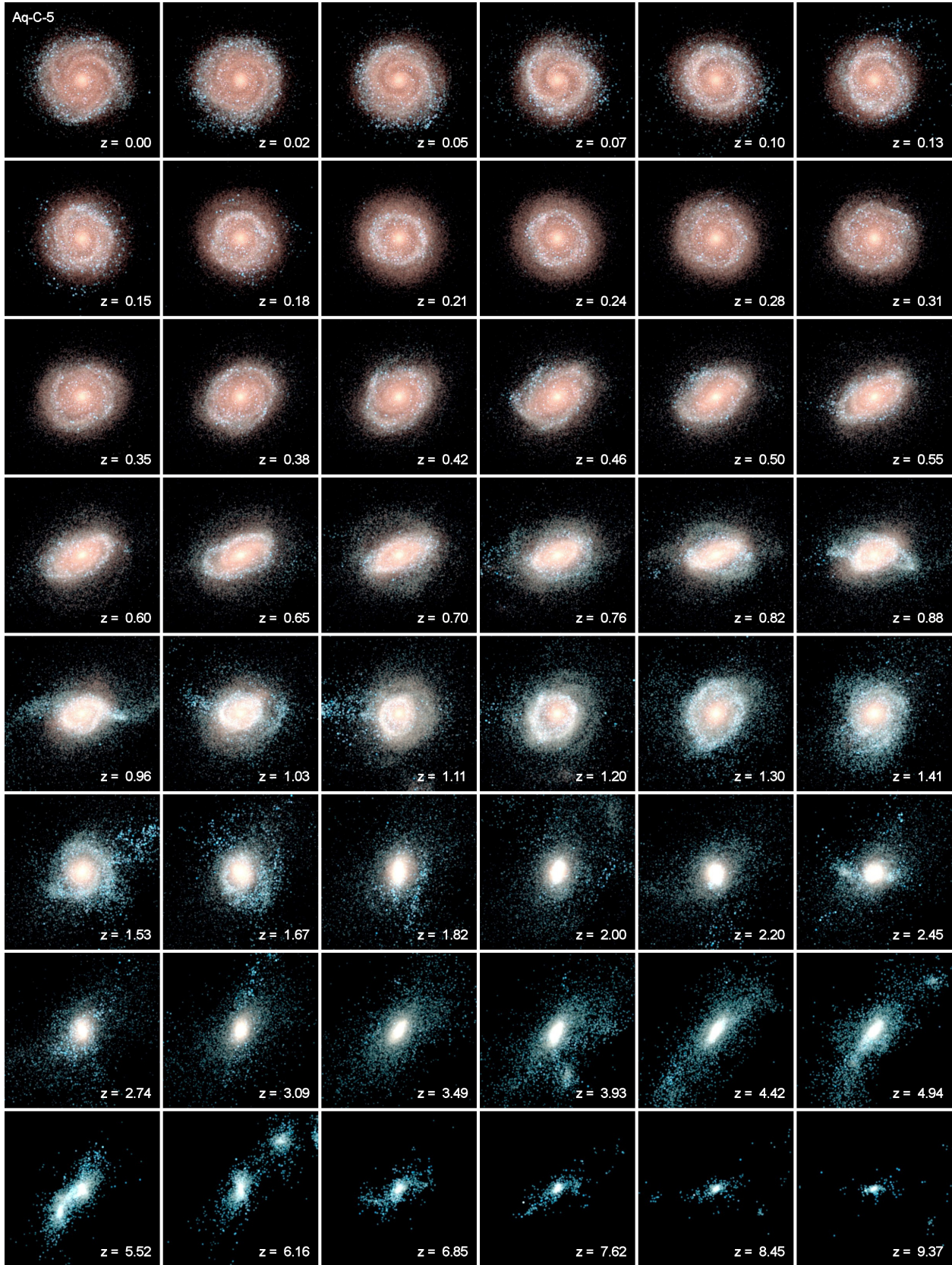
Figure 12. Time evolution sequence of the formation of the Aq-C-5 galaxy, from $z \sim 10$ to 0, as labelled. We show all stars in a box of length 50 kpc (physical) on a side, centred on the potential minimum of the main progenitor's dark matter halo. The $z = 0$ frame has been oriented for a face-on view, and this projection direction is kept in all other panels. Rest-frame stellar luminosities are mapped to image intensity and colour as in Fig. 1.
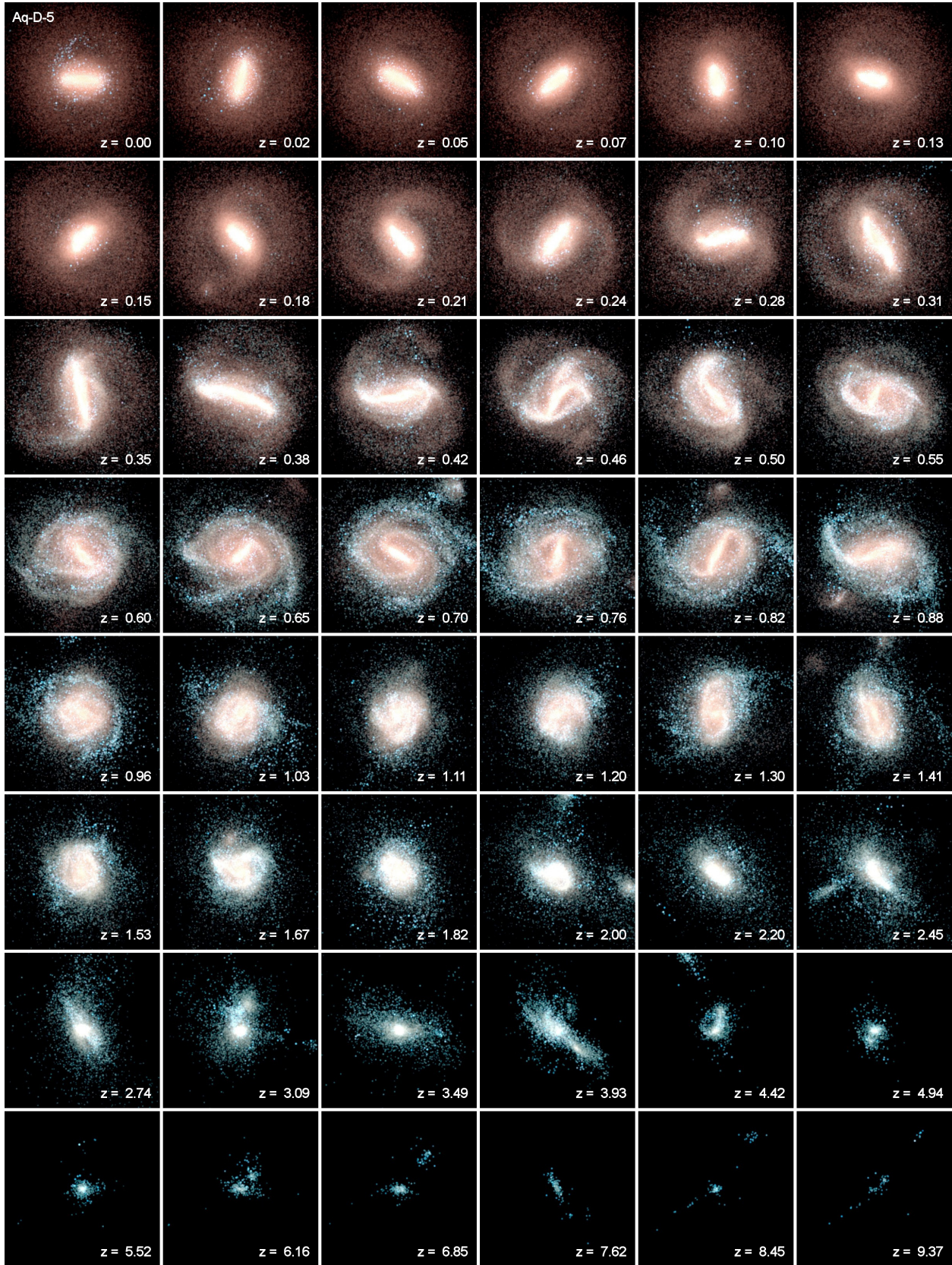
Figure 13. Time evolution sequence of the formation of the Aq-D-5 galaxy (as in Fig. 12, but for the Aq-D-5 simulation).
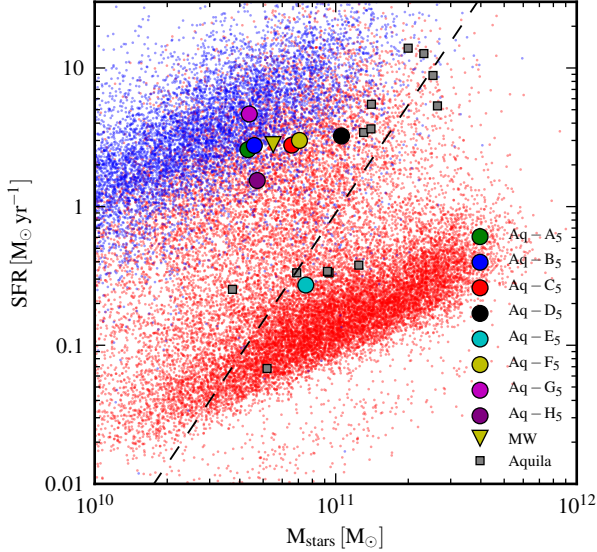
Figure 14. Present-day SFR, averaged over the past 0.5 Gyr, versus stellar mass. The coloured circles show the results of the simulations, while the down-pointing triangle marks the position of the Milky Way as given by Leitner & Kravtsov (2011). Background dots are a random sub-sample (10%) including only nearby galaxies ($z < 0.1$) of the SDSS MPA-JHU DR7. This sub-sample is divided into a blue cloud and a red sequence by adopting the same colour cut used in the Aquila project (Scannapieco et al. 2012). The small boxes show the results for the Aq-C halo obtained in the Aquila simulations. They tend to lie along the dashed line, which is systematically offset relative to the position of the Milky Way; once the stellar mass is small enough in the Aquila simulations, the present-day SFR is not sufficiently high.

width. Since we model the stellar mass return to the ISM in our simulations, the initial mass of each star particle (i.e., the mass that the particle has when it is created) is employed for the derivation of the SFRs. We used 100 bins of 140 Myr for a total time span of 14 Gyr. We additionally mark the formation rate of stars that have formed in situ in the main progenitor (blue histograms), or have been accreted from substructures (red histograms). The accreted stars are usually a small fraction, amounting to $\lesssim 10\%$ of the total stellar mass, with the notable exception of the Aq-F halo for which this fraction increases up to 23%. We also overplot the accretion rate of the central BH (green lines), determined as the average accretion rate between two simulation outputs and rescaled by a factor of $1/250$ to make it visible in the plots, to compare its formation history to that of stars. The general picture that emerges from this comparison is that of a connection between the two components, which show similar features in their formation histories at roughly the same look-back times. We address this point in more detail in Section 4.2.

From the figure it can be seen that SFHs come in a variety of shapes, that reflect the underlying mass assembly history of the haloes. The general trend is that of a peak of the SFR at early times ($z \sim 3 - 5$), with typical maximum SFRs of the order of $20\,\mathrm{M_\odot yr^{-1}}$, followed by a decline and a rather constant SFR at $z \lesssim 1$, with most of our galaxies ending up with SFRs of $\sim 2 - 3\,\mathrm{M_\odot yr^{-1}}$ at $z = 0$. However,

there are many exceptions to this rule, especially in systems where a large bulge is found at present times. In these cases the SFR tends to peak below $z \sim 1$ and then to drop quite abruptly (see haloes Aq-D, Aq-E and Aq-F). This can either be a signature of a strong merger event, a significant tidal perturbation or the result of secular evolution that triggers a bar instability. Another interesting case is that of the halo Aq-G, which features unusually little star formation at high redshift, a period of quite low star formation in the redshift interval $1 - 3$ followed by quite intense star formation from $z = 1$ to the present, and finally a merger even right at the present time that triggers a $z \simeq 0$ increase of the SFR. This history implies a quite young age of this galaxy.

This expectation is borne out in Fig. 16, which compares the mean mass-weighted stellar ages of our galaxies with SDSS data, as a function of stellar mass. Here, the galaxy Aq-G has indeed the youngest stellar population. It also has one of the smallest stellar masses among our set, making it in fact agree rather well with the observational determination of the age-stellar mass relation of late-type galaxies in the SDSS carried out by Gallazzi et al. (2005). Our other galaxies also agree well with these measurements, but our dynamic range in galaxy mass is too small to say whether we also reproduce the significant decline in age towards smaller stellar masses seen in the observations.

Based on the kinematic D/B decomposition carried out in Section 3.1, we can also determine the mean stellar ages of these components individually. As expected, the bulge components tend to be old; they have mean mass-weighted ages of $\sim 7 - 8$ Gyr, while the stellar disc components are on average younger with mean ages of the order of $\sim 4 - 5$ Gyr. Given also the general shape of the SFH curves, this suggests that bulge formation is associated with the early peak in the SFR while discs are built in a more gradual way at later times, consistent with the inside-out picture of Fall & Efstathiou (1980).

Of particular interest is how the stellar masses compare to the total virial masses of haloes. This is seen in Fig. 17, where we compare all of our simulations against the stellar mass-halo mass relation (dotted line) derived by Guo et al. (2010) from abundance matching arguments. The shaded region around the expected relation is determined such that its upper and lower boundaries are at ± 0.2 dex from the fiducial values, while the dashed line shows the baryonic content of a halo of a given virial mass if the universal baryon fraction is assumed. For each system, we include the results at a range of output times, from redshift $z = 2$ to 0, such that a continuous track is formed. As the abundance matching results only weakly depend on redshift (Behroozi et al. 2010; Moster et al. 2010), this then also gives a useful test to see whether our galaxies evolve consistently with this expected relation. We note that extending this test to still higher redshift would require taking into account the residual redshift dependence of the abundance matching results and the different growth histories of our haloes.

Reassuringly, the stellar masses of our systems are indeed small enough to be consistent with abundance matching arguments, although a subset of our galaxies is at the upper end of what is acceptable within the expected scatter. A good match is even obtained for two of the more massive galaxies of the sample, namely Aq-A and Aq-C, which have virial masses of almost $2 \times 10^{12}\,\mathrm{M_\odot}$ but still manage
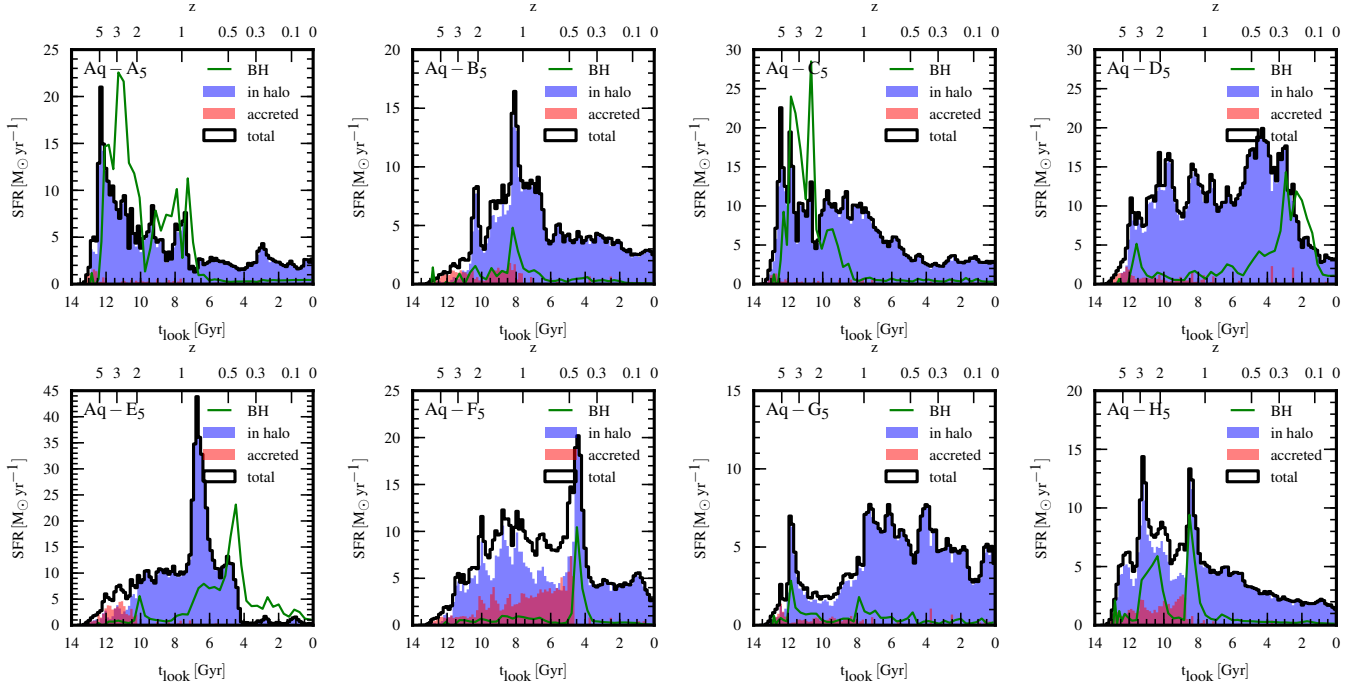
Figure 15. SFHs, as a function of look-back time and redshift, for the eight Aquarius haloes. Only stars within $r < 0.1\ r_{200}$ at $z = 0$ were considered in the measurement. For each halo, the total SFR is split between the contributions of stars born in the halo's most massive progenitor (blue histograms) and those that were accreted from other haloes or substructures within the halo (red histograms). The latter component is usually a small fraction of the total stellar mass, i.e. most stars of the galaxies form in situ. We also overplot the growth history of the supermassive BH residing at the centre of each galaxy (green lines). The growth rate is the average growth rate between two simulation outputs, scaled by a factor of $1/250$ to give them a comparable size as the SFRs (in solar masses per year).

to have a sufficiently small stellar mass and to form an extended disc. Matching the stellar mass-halo mass relation has not been achieved in the Aquila comparison project, except for runs G3-TO, G3-CR and R-AGN, which however did not form realistic disc systems with the employed implementations of strong feedback. Also, as pointed out by Guo et al. (2011) and Sawala et al. (2011), previous simulations – even the most successful ones among them – had generally failed to match this relation. Only very recently, a few studies (Guedes et al. 2011; Aumer et al. 2013; Stinson et al. 2013a) have reported successful simulations of individual galaxies conforming with the stellar mass-halo mass relation. Similar to our work, these successes have ultimately become possible due to an increased feedback strength and a more efficient coupling of the feedback energy to the gas phase. However, we note that most of these works employed halo masses considerably less massive than used here, typically around $\sim 0.7 \times 10^{12}\ \mathrm{M}_\odot$. This lower mass makes it easier to suppress star formation. A case in point is provided by the high-mass systems in Aumer et al. (2013), which show overly high low-redshift star formation, whereas their lower mass systems do not have this problem. To the best of our knowledge, our runs are the first examples of the successful formation of late-time spirals in haloes in the mass range $1 - 2 \times 10^{12}\ \mathrm{M}_\odot$, which is the size of the Milky Way.

4.2 Central black hole growth

In Fig. 18, we compare the BH mass growth to the stellar mass growth as a function of look-back time and redshift. The stellar mass growth curves are obtained by summing the masses of all the stellar particles within 10% of the halo virial radius at any given look-back time, while the BH masses are those of the most massive BH in the halo progenitor again at any given time. For all the haloes the two curves exhibit similar features. Both components show a steady growth over cosmic time, starting with a rapid growth rate at high redshift that subsequently flattens at low redshift ($z \lesssim 1$). These similarities in the general behaviour are indicative of a co-evolution between the stellar content of a galaxy and its central BH, consistent with the observed relation between the masses of the two components (e.g. Magorrian et al. 1998; Häring & Rix 2004).

This is not entirely unexpected since the growth of both components relies on the supply of the same fuel (i.e. gas), but it is not immediately obvious why two processes, such as star formation and gas accretion on to a BH, occurring on vastly different physical scales (the star-forming disc and the circumnuclear regions of a galaxy) should be so tightly related (for a recent review see Kormendy & Ho 2013). In fact, different conjectures have been made about the cause for the observed apparent co-evolution and tight galaxy – BH relations, ranging from feedback-regulated BH growth to statistical averaging as a result of successive mergers. We recall that our simulations are based on a local model for feedback-regulated growth of BHs through gas accretion.
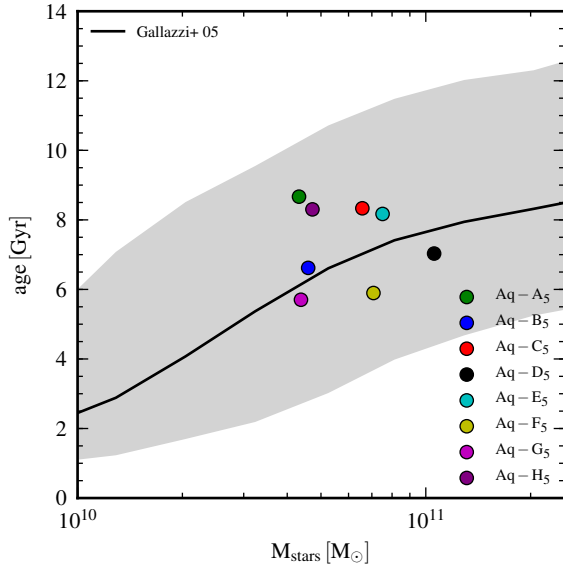
Figure 16. Mass-weighted stellar age versus stellar mass for our simulated galaxies at $z = 0$, compared to the median observational relation by Gallazzi et al. (2005). The grey band indicates the region between the 16th and 84th percentiles of the observed age distribution as a function of the stellar mass.
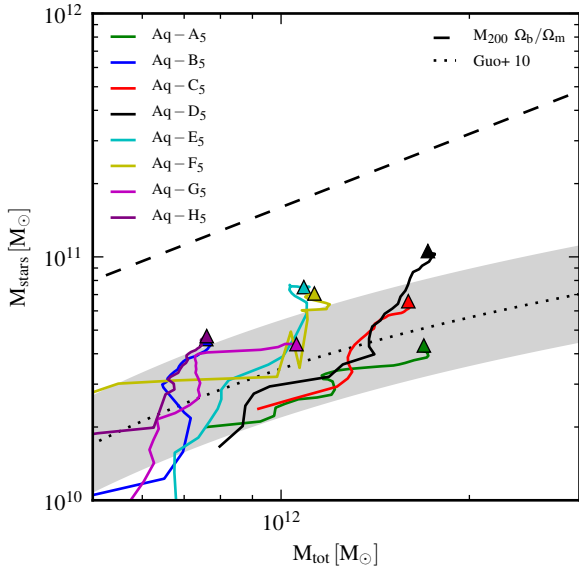
Figure 17. Stellar mass versus halo mass for the eight Aquarius haloes. The evolutionary tracks are plotted from $z = 2$ to the present time. The dashed line represents the baryonic mass associated with the halo if the universal baryon fraction is assumed. The dotted line shows the results obtained by abundance matching (Guo et al. 2010) and the grey region encloses an uncertainty of ± 0.2 dex around the mean value predicted by abundance matching. The evolutionary tracks of the haloes are in good agreement with abundance matching expectations, although there is a tendency of a slight overproduction of stars in a subset of our systems at $z = 0$.

This produces a quite close co-evolution of the BH mass and the stellar mass in galaxies, as seen in Fig. 18.

A closer inspection of the figure reveals however a difference in the slope of the evolutionary curves, especially at late times, where the BH mass in the majority of cases grows more slowly than the stellar mass, as can be inferred from the mass ratios between stellar mass and BH mass indicated at selected redshifts in the individual panels. This implies that our simulations typically predict a higher BH mass to stellar mass ratio at high redshift than seen in the local Universe. There is tentative observational evidence that this may indeed be the case; unusually large BH masses have for example been discovered in galaxies in the local Universe that are structurally similar to galaxies at much earlier times (van den Bosch et al. 2012). Another feature that can be seen in the evolution of the BH masses is the occurrence of merger events. They appear as sudden increases (almost in a step-like fashion) in the mass assembly history of the BHs, caused by brief phases of exponential Eddington-limited BH growth. Similar features are present, but less visible, in the stellar mass evolution curves as well.

All of the BHs in our galaxies end up with relatively high masses around 10^8 M$_\odot$, which are however still consistent with the BH mass-stellar mass relation of Häring & Rix (2004). The fact that we get reasonable BH masses together with realistic disc properties in self-consistent cosmological simulations represents an important achievement of our galaxy formation model. This is especially noteworthy as other BH feedback schemes are known to negatively impact galaxy morphologies. For example, in Haas et al. (2013) the gaseous discs in $z = 2$ galaxies were lost once AGN feedback was activated. Similarly, in the Aquila comparison project (Scannapieco et al. 2012), the nice (but overly massive) disc formed by RAMSES was lost once BH feedback was activated.

5   HALO MASS STRUCTURE

In this section, we discuss the overall mass structure of our galaxies, as reflected for example in their rotation curves. This is interesting for at least two reasons. On the one hand, the inner shape of the rotation curves is arguably one of the two primary areas where significant 'small-scale tensions' between ΛCDM and observational data may be present (the other contentious area is the abundance, central structure and spatial distribution of satellites, a topic beyond the scope of this paper). On the other hand, baryonic effects have recently been claimed to substantially affect the central dark matter structure, even in large spiral galaxies (Macciò et al. 2012). The claimed effect of strong, repetitive outflows originating in supernova feedback is that of introducing a dark matter core, thereby overcoming the adiabatic contraction of the halo that is usually expected as result of baryons cooling out in the centre. Given that our galaxies experience strong outflows, including repeated 'explosive' ones from strong quasar feedback, it is interesting to check to what extent we can confirm this finding in our simulations.
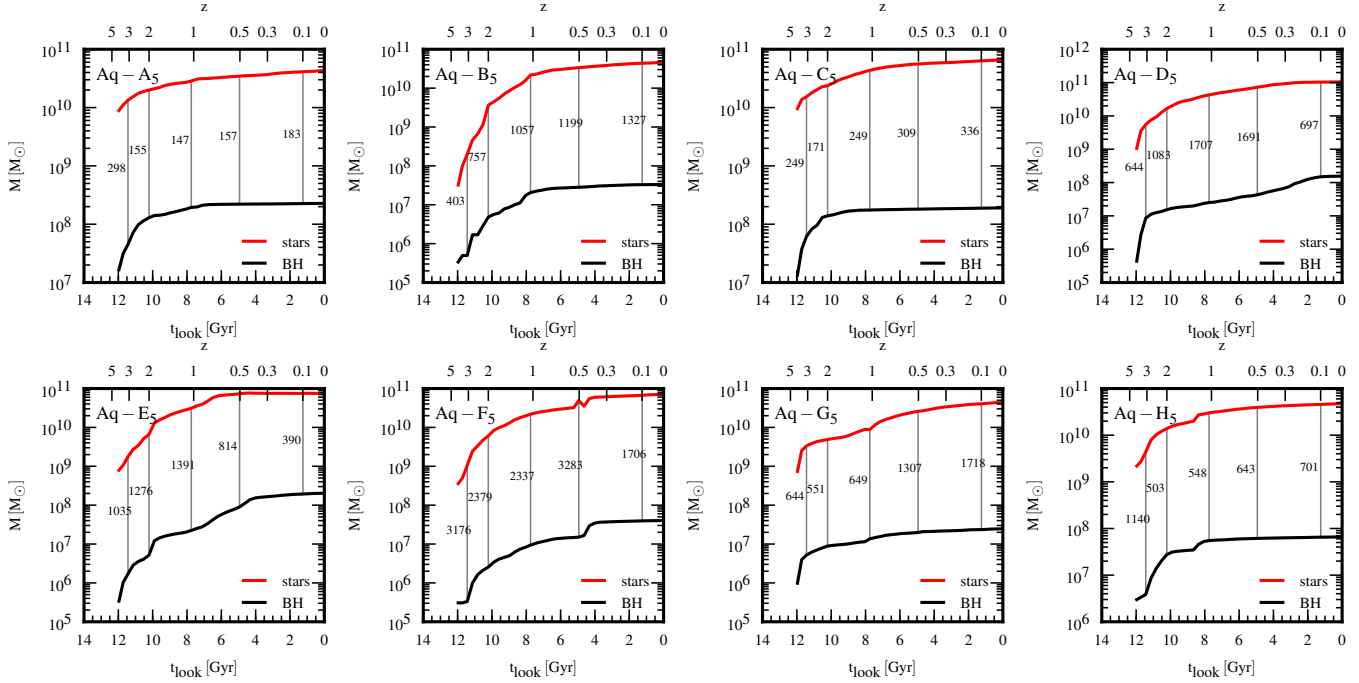
Figure 18. Evolution of the galaxy's stellar (red lines) and central BH (black lines) masses, as a function of look-back time and redshift, for the eight Aquarius haloes. The stellar masses are computed as the sum of the mass of each star particle within 10% of the halo virial radius at a given time, while for the BH we plot for any selected time the most massive BH present in the halo's most massive progenitor. The evolutionary trends show that both the stellar content and the BH mass of the simulated galaxies steadily grow with time, although the rate at which the mass is acquired usually declines at late times (see also Fig. 15). For each halo the mass assembly history of the two components shows similar features, supporting the notion of a (tight) link between them. The vertical lines and the associated numbers give the mass ratio of stars to central BH at a number of selected redshifts.
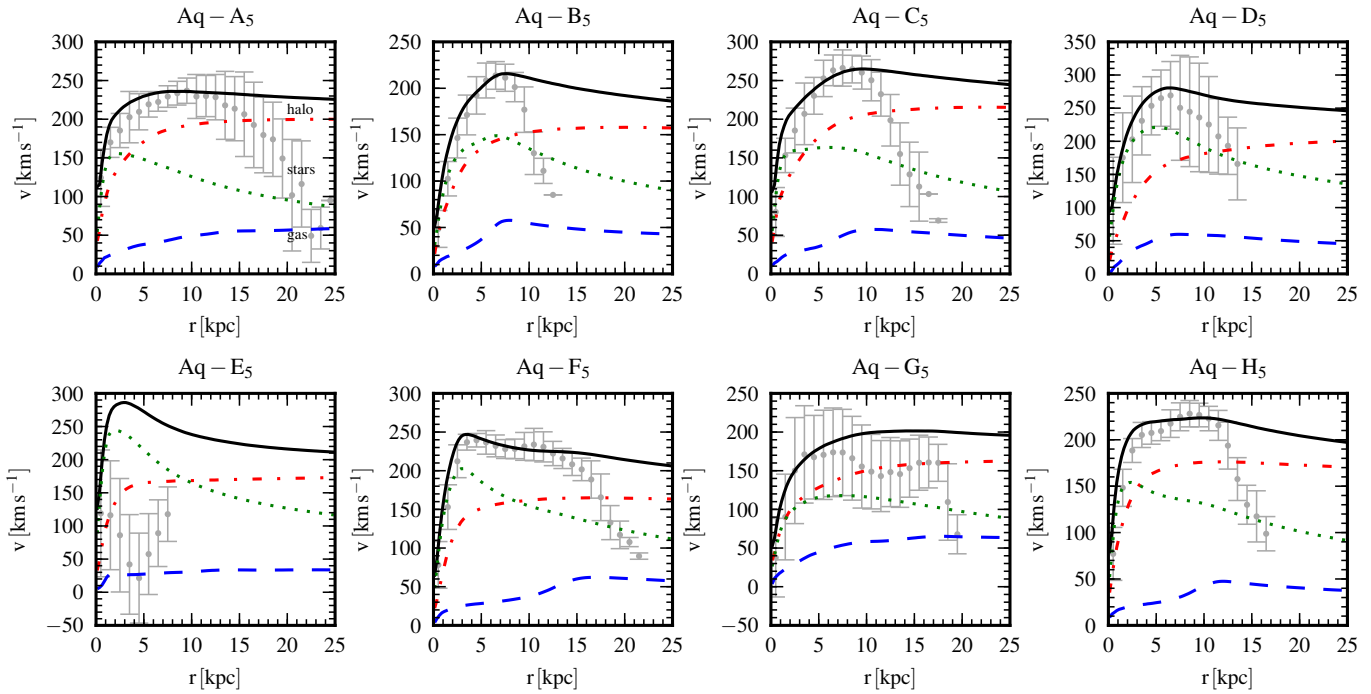
5.1 Rotation curves

The detailed shape of the rotation curve of a galaxy encodes key information about the mass distribution within the system. For instance, a pronounced peak of the rotation velocity in the innermost regions followed by a rapid decline is indicative of the presence of a massive and compact structure (often associated with a large, dominant stellar bulge in earlier simulation work of galaxy formation, see also Scannapieco et al. 2012), whilst late-type spirals are characterized by an almost flat profile of the rotational velocity which in the outer parts requires dark matter if the ordinary laws of gravity hold.

In Fig. 19, we present the rotation curves of our simulated galaxies. Contributions to the total rotation velocity (solid lines) have also been separately computed via $v_c(r) = \sqrt{GM(<r)/r}$ for the primary mass components that constitute each galaxy: stars (dotted lines), gas (dashed lines) and dark matter (dot-dashed lines). Points with error bars show instead the (mass-weighted) rotation velocity of cold star-forming gas within $0.1 \times R_{\rm vir}$ around the galaxy symmetry axis. With the exception of Aq-E, all galaxies have approximately flat rotation curves that show a rapid rise in the centre followed by a slowly declining trend after the maximum velocity has been reached. Baryons (in the form of stars) tend to dominate only in the innermost couple of kpc. However, for systems Aq-D, Aq-E and Aq-F this behaviour extends out to about 10 kpc and is responsible for the appearance of a more pronounced peak in the rotation

profiles. These galaxies have pronounced central bulges (and also the largest stellar masses), with Aq-E leading the set in this respect. Aq-G has the least massive stellar distribution in the inner parts and is dark matter dominated everywhere except for the innermost kpc.

For what concerns the gas component, its contribution to the circular velocity is quite subdominant but not completely negligible either, since velocities of up to ≈ 50 km s^{-1} are reached. Again, the exception is represented by the gas-poor system Aq-E, where only a maximum velocity of ≈ 35 km s^{-1} is attained. It is also interesting to note that the shapes of the gas rotation curves are rather different with respect to those of the other components, especially in systems Aq-B, Aq-C, Aq-F and Aq-H. This likely reflects a depletion of (cold) gas in the central regions due to the efficient star formation and associated feedback processes operating there. The actual kinematics of the gas closely follows the computed rotation velocity profiles, showing that the star-forming gas phase settles into a rotationally supported gaseous disc. In some of the haloes a sudden drop in the gas rotation velocity can be observed, and the radius at which this break occurs indicates the radial extension of the cold gas component.

Fig. 20 is complementary to Fig. 19 in the sense that it presents again the rotation curves of our simulated galaxies but this time the points with error bars show the rotation velocity of disc stars, that is stars with $r < 0.1 \times R_{\rm vir}$ and circularity parameter $\epsilon > 0.7$. Again, it is readily apparent

Figure 19. Rotation curves ($v_c(r) = \sqrt{GM(<r)/r}$) for the eight Aquarius haloes at $z = 0$. Different line types give the contributions of various mass components to the total circular velocity: stars (dotted lines), dark matter (dot-dashed lines) and gas (dashed lines). The total rotation curves are given by solid lines, while points with error bars show the rotation velocity of the star-forming gas within $0.1 \times R_{\rm vir}$. It is apparent that in most of the cases quite flat rotation curves are present. Some haloes (Aq-D, Aq-E and to a lesser degree Aq-F) however show that a spheroidal stellar structure (i.e., a bulge) still provides the dominant contribution to the circular velocity in the centre. The position of the sudden drop in the star-forming gas rotation velocity that can be observed in some of the haloes is set by the extension of this component.
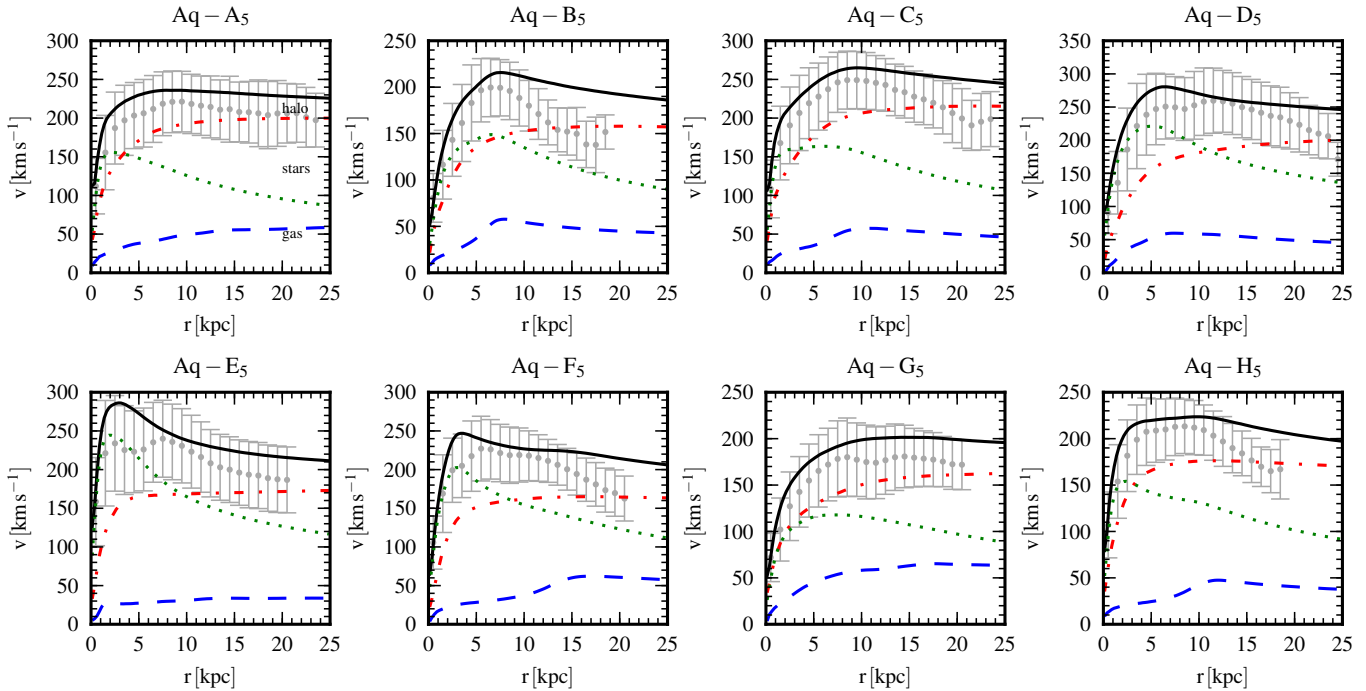
Figure 20. The same as in Fig. 19 but points with error bars represent the rotation velocity of disc stars selected by considering only stars within $0.1 \times R_{\rm vir}$ and circularity parameter $\epsilon > 0.7$. The figure shows that disc stars are indeed rotationally supported.
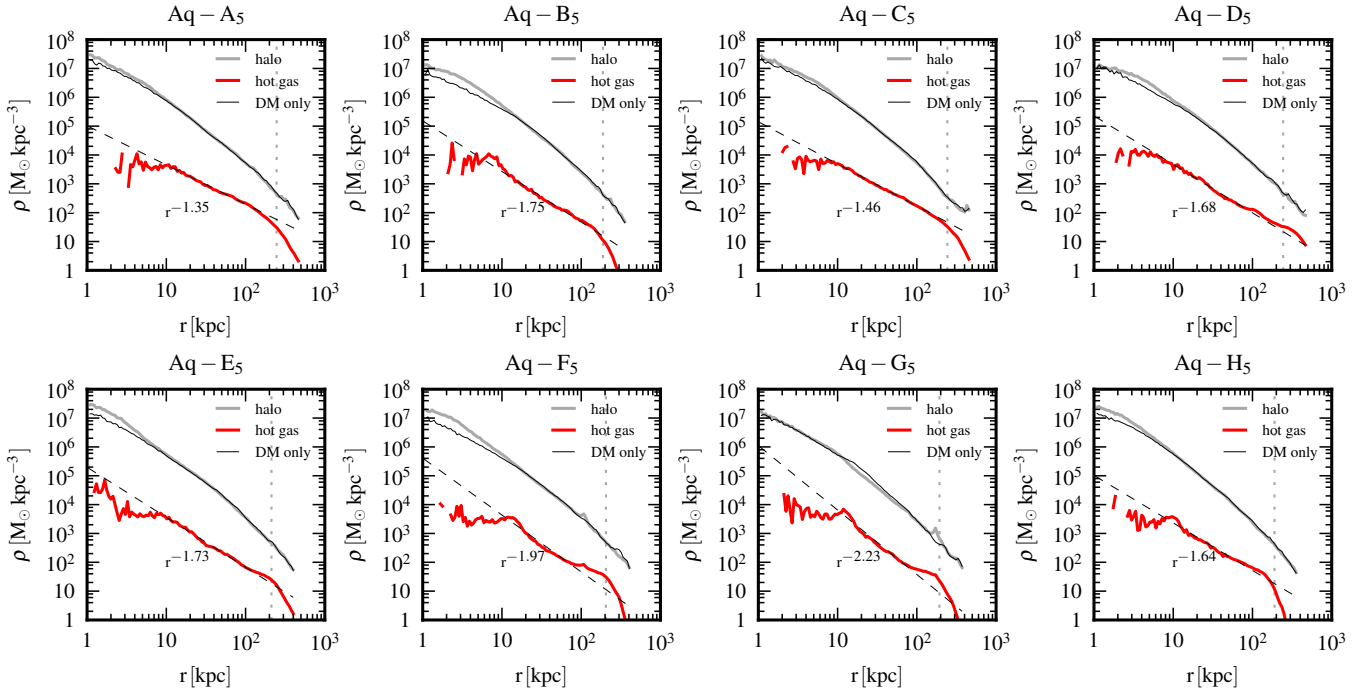
Figure 21. Spherically averaged dark matter (grey lines) and hot gas ($T > 3.0 \times 10^5$ K, red lines) density profiles of the eight simulated haloes. The density profiles obtained in the pure dark matter simulations (thin black lines) of the same haloes, rescaled by the factor $1 - \Omega_{\rm b}/\Omega_{\rm m}$, are also shown for comparison. The dotted vertical lines indicate the position of the virial radius of each halo. The contraction of the dark matter haloes due to the cooling and the infall of baryons in the central regions can be clearly detected in the majority of the simulated objects, whereas there is no sign of dark matter core formation in any of the galaxies. In the radial range between $\sim 10\,{\rm kpc}$ and the virial radius, the hot gas follows to good approximation a power-law profile (dashed lines), $\rho_{\rm hot}(r) \propto r^\alpha$, with α varying between -1.35 and -2.2 in the different systems.

that disc stars chosen according to this kinematic criterion comprise a rotationally supported structure.

5.2 Baryonic physics impact on dark matter

The modification of the dark matter structure of a Milky Way-sized halo due to baryonic effects is an extremely interesting, and so far unsettled question. While dark matter only simulations of Milky Way-sized haloes can be viewed as quite reliable these days, with several groups reaching consistent results independently and with different methods (e.g. Springel et al. 2008; Stadel et al. 2009), the situation with respect to baryons is far less clear. Navarro et al. (1996) were the first to demonstrate with N-body simulations that a sudden loss of a large fraction of the baryonic component from a dwarf galaxy halo could imprint a (small) dark matter core. Gnedin & Zhao (2002) however showed that even for assumptions of maximum feedback the central halo cusp could not be destroyed by outflows, with the inner density lowered only by a moderate factor. A similar conclusion was reached by Ogiya & Mori (2011). Mashchenko et al. (2006) argued that a larger impact is possible if there are strong random bulk motions of baryons in dark matter potentials in the early Universe, an idea that has recently gained popularity. Several studies have argued that baryonic effects can induce through this process dark matter cores in dwarf galaxies (Governato et al. 2010, 2012; Pontzen & Governato 2012), or even in large Milky Way size haloes or galaxy clusters (Macciò et al. 2012; Martizzi et al. 2013).

However, the recent work by Garrison-Kimmel et al. (2013) questions these results. There is simply not enough energy available in supernovae to achieve the reported dark matter flattenings. Also, cyclic blow outs are not necessarily more effective than a single large burst.

We provide here a simple first analysis of this important issue, which has also significant bearings on dark matter indirect detection in the Galaxy (e.g. Yang et al. 2013). In Fig. 21, we show spherically averaged dark matter density profiles for our eight different haloes (grey solid lines). We compare them to corresponding runs carried out with the same initial conditions but using dark matter alone (black thin lines). In these comparison simulations the baryons behave effectively as if they were dark matter as well. To make the comparison of the dark matter profiles more direct, we rescale the measured dark matter density of the latter runs by the factor $1 - \Omega_{\rm b}/\Omega_{\rm m}$, where $\Omega_{\rm b}$ and $\Omega_{\rm m}$ are the density parameters of baryons and dark matter in our hydrodynamical models, respectively. In this way, any difference in the recovered dark matter density profiles in the two sets of runs can be ascribed to the influence of baryonic physics alone. We see that in all cases the central dark matter density of our simulations that include baryons is *increased*, showing the expected effect for a mild adiabatic contraction. There is no trace of core formation in our results, despite the fact that we have substantial early feedback from winds and repeated quasar-driven outflows. These are apparently not sufficiently strong to trigger the alleged process of core formation, a
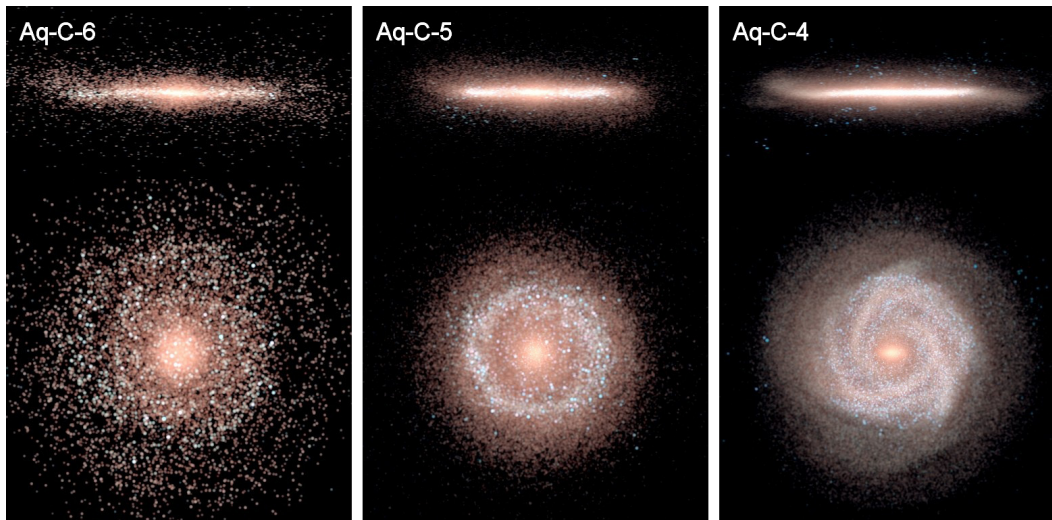
Figure 22. Stellar disc morphologies for the simulations Aq-C-6, Aq-C-5 and Aq-C-4 (from left to right, respectively). As in Fig. 1, the three panels feature an edge-on (top) and a face-on (bottom) view of the projected stellar density to allow a visual comparison of the disc structure and its composition in terms of stellar age as a function of the resolution.

finding consistent with the recent analysis of idealized test simulation by Garrison-Kimmel et al. (2013).

In Fig. 21, we also include measurements of the spherically averaged density profiles of the hot ($T > 3 \times 10^5$ K) gas component in our hydrodynamical simulations. This gas component forms a pressure-supported atmosphere, known as corona, which is nearly in hydrostatic equilibrium with the dark matter potential. The hot corona is rather extended, reaching distances up the halo virial radius (the vertical dotted lines in the figure) and beyond. The slope of its density profile is in general shallower than that of the dark matter, with a tendency of forming an approximately constant density state in the central regions ($r \lesssim 10$ kpc) where the galaxy is located. Compared to the Eris simulation (Guedes et al. 2011), our hot gas profiles have considerably steeper profiles; none is as strongly flattened as Eris, which shows a power-law profile with slope -1.13 over a similar radial range as our simulations.
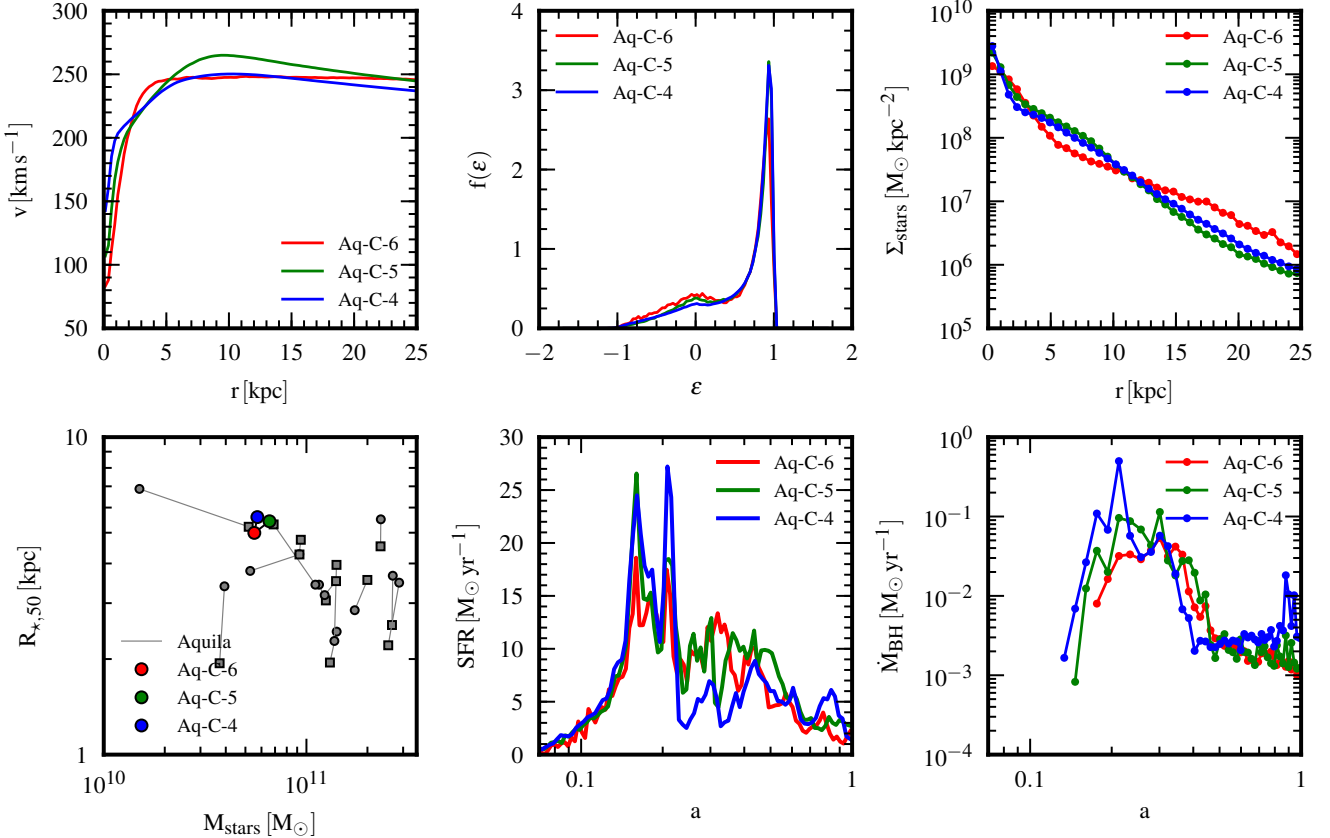
6   RESOLUTION STUDY

It is interesting to examine how robust our results are to changes in numerical resolution when *the same halo* is simulated at drastically different mass resolution. Experience shows that the high non-linearity of the feedback loops needed to tame star formation in Milky Way-sized haloes make the numerical results often less robust than is desirable when the resolution is changed. The Aquarius systems are ideal for examining this issue as the high quality of the initial conditions has been validated to high accuracy with dark matter only simulations.

To allow a straightforward comparison with the Aquila code comparison project we focus on the Aq-C system, which we have simulated both at eight times higher (Aq-C-4) and eight times lower (Aq-C-6) mass resolution than used in our default set up. In Fig. 22, we compare the stellar morphology we obtain for these three cases. The images are constructed

in the same way as those shown in Fig. 1, and use the same mapping of stellar luminosity to image intensity and colour. We have opted to show the $z = 0.2$ output instead of $z = 0$, because the Aq-C-4 run experiences a close tidal encounter with a massive satellite at around this time, which subsequently affects the ongoing star formation in Aq-C-4 and temporarily restricts it to a narrow inner ring. This changes the appearance of new young blue stars significantly, reducing the good visual correspondence of the systems Aq-C-5 and Aq-C-4 right at the particular output time of $z = 0$, which is a bit misleading given the overall good agreement of the runs. We note that also in the Aquila comparison project, a late time merger in the Aq-C system complicates the comparison of the different simulations as the exact timing and orbit of this incoming substructure depends sensitively on simulation details.

More quantitatively, in Fig. 23 we compare several different basic quantities and examine how they compare with each other in our Aq-C-4, Aq-C-5 and Aq-C-6 simulations. We consider the rotation curves, eccentricity distributions, surface mass density profiles, the relation between stellar half-mass radius and stellar mass, SFR history and BH growth history. We find that the eccentricity distribution converges particularly well, which is reassuring. This suggests that the overall morphology is quite robustly predicted by our simulation methodology, even at the comparatively low resolution of Aq-C-6. Also, the stellar surface mass density profiles converge quite well, especially between the higher resolution simulations Aq-C-5 and Aq-C-4. The low-resolution run shows still a quite similar disc profile, which is however slightly flatter. Similarly, the rotation curves exhibit very similar shape with only small deviations around the bulge and peak regions. Finally, the growth histories of the stars and the galaxy's supermassive BH show good overall agreement, with well-aligned patterns for the most important star bursts and merger events. This demonstrates that our simulations reliably and reproducibly track the same formation history of the Aq-C galaxy despite a variation of the

Figure 23. Comparison of the results obtained for the Aq-C halo at three different levels of numerical resolution, spanning a dynamic range of 64 in mass: Aq-C-6 (red), Aq-C-5 (green) and Aq-C-4 (blue). The six panels show: the circular velocity profiles (top left), the circularity distributions of stellar orbits (top middle), the stellar surface density profiles (top right), the relation between stellar half-mass radius and stellar mass (bottom left), the SFR history (bottom middle) and finally, the growth rate of the central supermassive BH (bottom right). In the comparison of $R_{\star,50}$ with $M_{\rm stars}$, we include the simulation results of the Aquila comparison project for the same Aq-C halo, and simulations carried out at different numerical resolution (indicated by squares for level 5 and circles for level 6) but with the same code, and physical models are connected by thin lines.

mass resolution over a factor of 64, and despite the presence of very strong negative (winds and BH growth) and positive (enhanced cooling due to metal enrichment) feedback.

The lower-left panel in Fig. 23 shows our three different resolution simulations as symbols in the half-mass – stellar mass plane. The three runs of the Aq-C object are connected by thin lines, forming a small triangle. For comparison, we also include in the figure the results of all the Aq-C simulations carried out in the Aquila comparison project, which employed a large set of other simulation codes and feedback models. In Aquila, the two lower resolutions corresponding to Aq-C-6 and Aq-C-5 were considered, and we include these results as symbols (circles for level 6 and squares for level 5), connecting each pair of runs carried out with the same code by a thin line. Note that the sides of the small triangle we obtained for our AREPO runs are shorter than any of the connecting lines for other codes, highlighting the good convergence properties of our simulation methodology relative to other implementations. Especially, the galaxy sizes appear to be more robust in our code than in other implementations of the galaxy formation physics. This good convergence for galaxy sizes can be interpreted as circumstantial evidence that angular momentum conservation, which is not manifest in mesh codes, is sufficiently accurate in our simulations. Interestingly, two simulations from the Aquila project reached almost the same combination of stellar mass and galaxy size as found in our simulations. These are the GADGET3 run with BHs (GR-BH) and the RAMSES run with AGN-feedback (R-AGN), both at resolution level 5. However, these simulations formed a dominant spheroid with at best a feeble disc component. The majority of the Aquila galaxies was however simply too massive, by up to a factor of ~ 5, and also too compact given their stellar mass.

7 DISCUSSION

7.1 Comparison with previous studies

Previous studies, in particular the Aquila comparison project (Scannapieco et al. 2012), have shown that the formation of disc galaxies hinges strongly on the relative level of star formation at early and late times. In fact, there is a

clear correlation in the sense that the more successful models are those which manage to suppress high-redshift star formation while still allowing efficient star formation at late times. The difference this makes is particularly evident in a comparison of the results of Scannapieco et al. (2009) and Aumer et al. (2013) which partially overlap in the set of objects studied and use largely the same numerical techniques, except that Aumer et al. (2013) invoke an additional strong feedback channel in order to account for 'early stellar feedback'. The difference in the results they obtain is striking. While in Scannapieco et al. (2009) none of the galaxies contain more than 20 per cent of the total stellar mass in their discs, Aumer et al. (2013) achieve the highest D/B ratios reported in the literature thus far, with values for D/T as large as ~ 0.6. This is comparable to what we reach here.

The disc fractions reported by Guedes et al. (2011) and Agertz et al. (2011) are similarly high but are based on photometric decompositions, which is known to produce inflated disc fractions compared to kinematic decompositions (e.g. Scannapieco et al. 2011). We note that the Eris simulation did not include high temperature metal cooling, an effect that would have significantly boosted cooling, given that outflows are strong in Eris. The galaxy studied by Agertz et al. (2011) has accounted fully for metal-line cooling (as we do) and promptly obtained rotation curves peaks that are too high, indicating still too efficient cooling and a stellar content inconsistent with abundance matching results. A similar, albeit more severe problem is seen in the recent simulations reported by Few et al. (2012) based on the RAMSES code, which feature quite well-defined discs but also rotation curves rising to the centre as a result of overly luminous bulges.

It is worth stressing that our simulations study the same initial conditions as in Scannapieco et al. (2009) and (in part) in Aumer et al. (2013), but use a fundamentally different numerical method and a radically different treatment of feedback processes. In particular, we do not invoke early stellar feedback, rather we resort to supernova-driven outflows, modelled as energy-driven winds whose velocity is tied to the characteristic velocity of haloes. The efficiency of this process is assumed to be close to the upper envelope of what is energetically plausible. We do not implement the feedback through a 'delayed cooling' approach that has become very popular in recent times in cosmological simulations of galaxy formation (Stinson et al. 2006; Guedes et al. 2011). As has been pointed by Agertz et al. (2013), the present implementations of these schemes appear to considerably exaggerate the impact of the Type II supernova energy input they are meant to mimic. It also needs to be seen whether the optimistic assumptions made about the efficiency of radiative pressure feedback from early stars are plausible. Serious doubts about this seem justified (Krumholz & Thompson 2013).

We note that we do not use the high star formation threshold advocated by Governato et al. (2010) and Guedes et al. (2011). Hence, this is not a unique requirement to form realistic disc galaxies, even though it may still be essential within a certain numerical framework for treating hydrodynamics, star formation and feedback. Our feedback model follows the philosophy of an explicit subgrid model that does not require model adjustments when the numerical resolution is changed. While physical processes that are subgrid (such as the formation of individual stars or the launching of the galactic wind) remain unresolved when the resolution is increased, this approach allows numerically and physically well-posed simulation schemes with results that do not strongly depend on numerical resolution. This is highly desirable to obtain meaningful results in cosmological structure formation, where invariably galaxies of widely different mass form concurrently.

Another interesting point to observe is that the haloes of most of our galaxies are considerably more massive than those of the best successful disc galaxies reported in the literature thus far. When accounting for the different virial mass definition adopted by Eris (which gives $\sim 15\%$ higher values than M_{200}), in fact *all* of our haloes are more massive than Eris and the g1536 halo of Stinson et al. (2013a). It becomes more difficult to control excessive star formation in such larger haloes, and we consider it to be a success of our model that this is possible in haloes above $10^{12}\,\mathrm{M}_\odot$. Only Aumer et al. (2013) have reported good discs in such more massive haloes, but their simulations tend to show too high SFRs at low redshift in the corresponding galaxies, a problem that our simulations do not have, in part due to the inclusion of AGN feedback. Also their high mass galaxies at $z = 0$ appear to be too small, and the trend between stellar mass and size is too flat.

7.2 Conclusions

Our simulations are probably the most successful hydrodynamical simulations of the formation of Milky Way-like galaxies within a full cosmological context published thus far. The models Aq-C and Aq-F are the best Milky Way look alikes among our set. They feature galaxies with high D/T ratio that form in sufficiently massive dark matter haloes to qualify as Milky Way systems. At the same time, these galaxies have a stellar mass, a current SFR, a rotation curve, a size and a present-day gas fraction in reasonable agreement with properties of the Milky Way. Our models are also the first successful disc formation runs that simultaneously grow a supermassive BH of reasonable size even though back-reaction on the forming galaxies through strong AGN feedback is included. The final BH masses we obtain tend to be significantly higher than the mass of Sagittarius A* in the centre of the Milky Way. This disagreement may not be very profound since it is well known that Sagittarius A* is undermassive with respect to what is expected from the local BH mass scaling relations (Häring & Rix 2004), which our BH model is designed to match. The discrepancy could be rectified by assuming a higher coupling efficiency for the BH feedback. The self-regulated nature of the BH growth would then still inject the same energy – and leave the galaxy properties to first order unchanged – but achieve this with a smaller BH mass growth. However, the good match to the BH mass scaling relations may then be lost.

As shown by Vogelsberger et al. (2013) and Torrey et al. (2013), the simulation methodology used here also produces very promising results for the galaxy population as a whole. This suggests that hydrodynamical studies of galaxy formation in large volumes, and at extremely high resolution in individual haloes, are finally turning into serious competition for semi-analytic models of galaxy formation in terms of their ability to predict galaxies in reasonable agreement

with observational data. The higher physical fidelity of hydrodynamic simulations, especially when it comes to the dynamics of the diffuse gas phase, make them ultimately the superior tool for exploring and understanding galaxy formation physics. We note that our methods also represent a significant advance in computational efficiency compared to previous generations of hydrodynamical galaxy formation simulations, despite the fact that we employ a complicated unstructured moving-mesh code. Our simulation of Aq-C-4 has consumed less than 10^5 CPU hours on a cluster with Intel Sandy Bridge 2.7 GHz CPUs (2.7 GHz) and 512 MPI tasks, including all group finding and SUBFIND post-processing. We also recall the good numerical convergence of our approach, which to our knowledge is presently unmatched by other simulation methodologies in the field.

The near-term future of cosmological hydrodynamic simulations appears truly exciting. There are now several groups and codes that have made great strides towards forming realistic galaxies, both in cosmological simulations like the ones discussed here, and in simulations of isolated galaxies (e.g. Hopkins et al. 2012). This will be of enormous help for advancing our theoretical understanding of galaxy formation and for properly interpreting the wealth of observational data. However, the devil is very much in the details of feedback, and for the time being this remains a major headache which compromises some of the predictive power of simulations. A 'first principles' understanding of how galaxies form will ultimately require simulations that fully account for the physics of the ISM and the cosmological context at the same time, a truly formidable task for the future.

REFERENCES

Abadi M. G., Navarro J. F., Steinmetz M., Eke V. R., 2003, ApJ, 597, 21

Agertz O., Kravtsov A. V., Leitner S. N., Gnedin N. Y., 2013, ApJ, 770, 25

Agertz O., Teyssier R., Moore B., 2011, MNRAS, 410, 1391

Aumer M., White S. D. M., Naab T., Scannapieco C., 2013, MNRAS, 434, 3142

Balogh M. L., Pearce F. R., Bower R. G., Kay S. T., 2001, MNRAS, 326, 1228

Battaglia G., et al., 2005, MNRAS, 364, 433

Bauer A., Springel V., 2012, MNRAS, 423, 2558

Behroozi P. S., Conroy C., Wechsler R. H., 2010, ApJ, 717, 379

Boylan-Kolchin M., Springel V., White S. D. M., Jenkins A., Lemson G., 2009, MNRAS, 398, 1150

Boylan-Kolchin M., Springel V., White S. D. M., Jenkins A., 2010, MNRAS, 406, 896

Boylan-Kolchin M., Bullock J. S., Kaplinghat M., 2011, MNRAS, 415, L40

Boylan-Kolchin M., Bullock J. S., Kaplinghat M., 2012, MNRAS, 422, 1203

Boylan-Kolchin M., Bullock J. S., Sohn S. T., Besla G., van der Marel R. P., 2013, ApJ, 768, 140

Brooks A. M., et al., 2011, ApJ, 728, 51

Chabrier G., 2003, ApJ, 586, L133

Courteau S., Dutton A. A., van den Bosch F. C., MacArthur L. A., Dekel A., McIntosh D. H., Dale D. A., 2007, ApJ, 671, 203

Davis M., Efstathiou G., Frenk C. S., White S. D. M., 1985, ApJ, 292, 371

Dehnen W., McLaughlin D. E., Sachania J., 2006, MNRAS, 369, 1688

Dutton A. A., et al., 2011, MNRAS, 416, 322

Fall S. M., Efstathiou G., 1980, MNRAS, 193, 189

Faucher-Giguère C.-A., Lidz A., Zaldarriaga M., Hernquist L., 2009, ApJ, 703, 1416

Few C. G., Gibson B. K., Courty S., Michel-Dansac L., Brook C. B., Stinson G. S., 2012, A&A, 547, A63

Gallazzi A., Charlot S., Brinchmann J., White S. D. M., Tremonti C. A., 2005, MNRAS, 362, 41

Garrison-Kimmel S., Rocha M., Boylan-Kolchin M., Bullock J. S., Lally J., 2013, MNRAS, 433, 3539

Genel S., Vogelsberger M., Nelson D., Sijacki D., Springel V., Hernquist L., 2013, MNRAS, 435, 1426

Gnedin O. Y., Zhao H., 2002, MNRAS, 333, 299

Governato F., et al., 2004, ApJ, 607, 688

Governato F., Willman B., Mayer L., Brooks A., Stinson G., Valenzuela O., Wadsley J., Quinn T., 2007, MNRAS, 374, 1479

Governato F., et al., 2010, Nat., 463, 203

Governato F., et al., 2012, MNRAS, 422, 1231

Graham A. W., 2001, AJ, 121, 820

Graham A. W., 2002, MNRAS, 334, 721

Graham A. W., Worley C. C., 2008, MNRAS, 388, 1708

Guedes J., Callegari S., Madau P., Mayer L., 2011, ApJ, 742, 76

Guo Q., White S., Li C., Boylan-Kolchin M., 2010, MNRAS, 404, 1111

Guo Q., et al., 2011, MNRAS, 413, 101

Haas M. R., Schaye J., Booth C. M., Dalla Vecchia C., Springel V., Theuns T., Wiersma R. P. C., 2013, MNRAS, 435, 2955

Häring N., Rix H.-W., 2004, ApJ, 604, L89

Haynes M. P., Giovanelli R., Salzer J. J., Wegner G., Freudling W., da Costa L. N., Herter T., Vogt N. P., 1999a, AJ, 117, 1668

Haynes M. P., Giovanelli R., Chamaraux P., da Costa L. N., Freudling W., Salzer J. J., Wegner G., 1999b, AJ, 117, 2039

Hopkins P. F., Quataert E., Murray N., 2012, MNRAS, 421, 3488

Hummels C. B., Bryan G. L., 2012, ApJ, 749, 140

Katz N., Gunn J. E., 1991, ApJ, 377, 365

Kaufmann T., Mayer L., Wadsley J., Stadel J., Moore B., 2006, MNRAS, 370, 1612

Kaufmann T., Mayer L., Wadsley J., Stadel J., Moore B., 2007, MNRAS, 375, 53

Kereš D., Vogelsberger M., Sijacki D., Springel V., Hernquist L., 2012, MNRAS, 425, 2027

Kormendy J., Ho L. C., 2013, ARA&A, 51, 511

Krumholz M. R., Thompson T. A., 2013, MNRAS, 434, 2329

Leitner S. N., Kravtsov A. V., 2011, ApJ, 734, 48

Li Y.-S., White S. D. M., 2008, MNRAS, 384, 1459

MacArthur L. A., Courteau S., Holtzman J. A., 2003, ApJ, 582, 689

Macciò A. V., Stinson G., Brook C. B., Wadsley J., Couchman H. M. P., Shen S., Gibson B. K., Quinn T., 2012, ApJ, 744, L9

Magorrian J., et al., 1998, AJ, 115, 2285

Martig M., Bournaud F., Croton D. J., Dekel A., Teyssier R., 2012, ApJ, 756, 26

Martizzi D., Teyssier R., Moore B., 2013, MNRAS, 432, 1947

Mashchenko S., Couchman H. M. P., Wadsley J., 2006, Nat., 442, 539

Möllenhoff C., 2004, A&A, 415, 63

Moster B. P., Somerville R. S., Maulbetsch C., van den Bosch F. C., Macciò A. V., Naab T., Oser L., 2010, ApJ, 710, 903

Navarro J. F., Eke V. R., Frenk C. S., 1996, MNRAS, 283, L72

Navarro J. F., Steinmetz M., 2000, ApJ, 538, 477

Nelson D., Vogelsberger M., Genel S., Sijacki D., Kereš D., Springel V., Hernquist L., 2013, MNRAS, 429, 3353

Ogiya G., Mori M., 2011, ApJ, 736, L2

Okamoto T., Eke V. R., Frenk C. S., Jenkins A., 2005, MNRAS, 363, 1299

Piontek F., Steinmetz M., 2011, MNRAS, 410, 2625

Pizagno J., et al., 2007, AJ, 134, 945

Pontzen A., Governato F., 2012, MNRAS, 421, 3464

Power C., Navarro J. F., Jenkins A., Frenk C. S., White S. D. M., Springel V., Stadel J., Quinn T., 2003, MNRAS, 338, 14

Puchwein E., Springel V., 2013, MNRAS, 428, 2966

Robertson B., Yoshida N., Springel V., Hernquist L., 2004, ApJ, 606, 32

Sakamoto T., Chiba M., Beers T. C., 2003, A&A, 397, 899

Sales L. V., Navarro J. F., Schaye J., Dalla Vecchia C., Springel V., Booth C. M., 2010, MNRAS, 409, 1541

Sales L. V., Navarro J. F., Schaye J., Dalla Vecchia C., Springel V., Haas M. R., Helmi A., 2009, MNRAS, 399, L64

Sawala T., Guo Q., Scannapieco C., Jenkins A., White S., 2011, MNRAS, 413, 659

Scannapieco C., Tissera P. B., White S. D. M., Springel V., 2008, MNRAS, 389, 1137

Scannapieco C., White S. D. M., Springel V., Tissera P. B., 2009, MNRAS, 396, 696

Scannapieco C., White S. D. M., Springel V., Tissera P. B., 2011, MNRAS, 417, 154

Scannapieco C., et al., 2012, MNRAS, 423, 1726

Sérsic J. L., 1963, Bol. Asociacion Argentina de Astron. La Plata Argentina, 6, 41

Shen S., Mo H. J., White S. D. M., Blanton M. R., Kauffmann G., Voges W., Brinkmann J., Csabai I., 2003, MNRAS, 343, 978

Sijacki D., Vogelsberger M., Kereš D., Springel V., Hernquist L., 2012, MNRAS, 424, 2999

Sommer-Larsen J., Götz M., Portinari L., 2003, ApJ, 596, 47

Springel V., 2005, MNRAS, 364, 1105

Springel V., 2010, MNRAS, 401, 791

Springel V., Hernquist L., 2003, MNRAS, 339, 289

Springel V., Di Matteo T., Hernquist L., 2005a, MNRAS, 361, 776

Springel V., et al., 2005b, Nat., 435, 629

Springel V., Di Matteo T., Hernquist L., 2005c, ApJ, 620, L79

Springel V., Frenk C. S., White S. D. M., 2006, Nat., 440, 1137

Springel V., et al., 2008, MNRAS, 391, 1685

Stadel J., Potter D., Moore B., Diemand J., Madau P., Zemp M., Kuhlen M., Quilis V., 2009, MNRAS, 398, L21

Stinson G., Seth A., Katz N., Wadsley J., Governato F., Quinn T., 2006, MNRAS, 373, 1074

Stinson G. S., Bailin J., Couchman H., Wadsley J., Shen S., Nickerson S., Brook C., Quinn T., 2010, MNRAS, 408, 812

Stinson G. S., Brook C., Macciò A. V., Wadsley J., Quinn T. R., Couchman H. M. P., 2013a, MNRAS, 428, 129

Stinson G. S., et al., 2013b, MNRAS, preprint (arXiv:1301.5318)

Torrey P., Vogelsberger M., Sijacki D., Springel V., Hernquist L., 2012, MNRAS, 427, 2224

Torrey P., Vogelsberger M., Genel S., Sijacki D., Springel V., Hernquist L., 2013, submitted to MNRAS, preprint (arXiv:1305.4931)

Tully R. B., Fisher J. R., 1977, A&A, 54, 661

Uhlig M., Pfrommer C., Sharma M., Nath B. B., Enßlin T. A., Springel V., 2012, MNRAS, 423, 2374

van den Bosch R. C. E., Gebhardt K., Gültekin K., van de Ven G., van der Wel A., Walsh J. L., 2012, Nat., 491, 729

Verheijen M. A. W., 2001, ApJ, 563, 694

Vogelsberger M., Sijacki D., Kereš D., Springel V., Hernquist L., 2012, MNRAS, 425, 3024

Vogelsberger M., Genel S., Sijacki D., Torrey P., Springel V., Hernquist L., 2013, MNRAS, preprint (arXiv:1305.2913)

Wakker B. P., van Woerden H., 1991, A&A, 250, 509

Wang J., Frenk C. S., Navarro J. F., Gao L., Sawala T., 2012, MNRAS, 424, 2715

Wilkinson M. I., Evans N. W., 1999, MNRAS, 310, 645

Windhorst R. A., et al., 1991, ApJ, 380, 362

Xue X. X., et al., 2008, ApJ, 684, 1143

Yang R.-Z., Feng L., Li X., Fan Y.-Z., 2013, ApJ, 770, 127